Acta Materialia 306 (2026) 121918

Contents lists available at ScienceDirect

Acta Materialia

journal homepage: www.elsevier.com/locate/actamat

Full length article

Assessment of the thermodynamics, kinetics and crystallization sequence of Ni–Nb–P-based bulk metallic glass-forming alloys

Lucas M. Ruschel [a,*], Bastian Adam [a], Oliver Gross [a], Maximilian Frey [a], Nico Neuber [a], Fan Yang [b], Ralf Busch [a]

[a] Chair of Metallic Materials, Saarland University, Saarbruecken 66123, Germany
[b] Institute of Materials Physics in Space, German Aerospace Center (DLR), 51170 Cologne, Germany

ARTICLE INFO

Keywords:
Bulk metallic glass
Ni–Nb-based BMGs
Electrostatic levitation
Viscosity
Fragility
Crystallization

ABSTRACT

This study investigates the glass-forming ability of Ni–Nb–P-based bulk metallic alloys through a systematic analysis of their thermodynamic, kinetic, and crystallization behavior. Differential scanning calorimetry, viscosity measurements, and in-situ synchrotron X-ray diffraction were employed to examine three compositions: $Ni_{62}Nb_{38}$, $Ni_{59.2}Nb_{38.8}P_2$ and $Ni_{59.2}Nb_{33.8}Ta_5P_2$. While all alloys exhibit a high thermodynamic driving force for crystallization, the phosphorus- and tantalum-containing variants demonstrate significantly improved glass-forming ability. This improvement is linked to increased viscosity and suppression of primary crystallization. In particular, the addition of phosphorus promotes the formation of a phosphorus-rich intermetallic phase that requires long-range diffusion, delaying crystallization. The combined kinetic slowdown and delayed phase formation sufficiently retard crystallization, allowing fully amorphous samples up to 6 mm in diameter to be produced, compared to 2 mm for binary Ni–Nb. These findings highlight how judicious micro-alloying can enhance glass-forming ability through kinetic control of the crystallization pathway.

1. Introduction

Bulk metallic glasses (BMGs) represent a distinct class of metallic materials characterized by an amorphous atomic structure that lacks long-range translational symmetry. Due to the absence of grain boundaries and other crystallographic defects, BMGs exhibit a unique combination of properties such as high strength and hardness, enhanced corrosion resistance and, in some cases, favorable magnetic performance [1–3]. These characteristics have made BMGs attractive for a wide range of technological applications. However, the limited glass-forming ability (GFA) of most systems restricts the maximum size of fully amorphous components, posing a significant barrier to broader technological implementation.

Improving the GFA of metallic glasses has therefore become a central focus of alloy development. One widely adopted strategy involves designing compositions near deep eutectics and incorporating multiple elements with large atomic size mismatches and strong negative enthalpies of mixing. These features increase melt viscosity and promote short- and medium-range atomic order, which together suppress nucleation and growth of competing crystalline phases [4–6]. Among the known glass-forming systems, Ni-based BMGs have attracted particular attention due to their combination of high strength in the range of 3 GPa, elevated glass transition temperatures about 900 K and excellent corrosion resistance [7–9]. Within this class, the binary Ni–Nb system stands out by achieving a critical casting thickness of up to 2 mm at the close-eutectic composition $Ni_{62}Nb_{38}$ [10]. This has been considered exceptional for a binary metallic glass and makes it a valuable basis for further alloy optimization.

Recent work from our group has demonstrated that minor additions of P can significantly enhance both the glass-forming ability (GFA) and thermal stability of the Ni–Nb system. Critical casting diameters of up to 5 mm were achieved through targeted P alloying. Subsequent partial substitution of Nb with Ta led to a further improvement in GFA, yielding fully amorphous rods up to 6 mm in diameter, far exceeding the state of the art for Ni–Nb-based alloys [7,11,12]. Notably, micro-alloying does not significantly affect the mechanical properties, with only a slight reduction in fracture toughness that remains within the range of comparable brittle crystalline engineering materials, making these alloys highly promising for industrial applications [13–16].

The present study expands on previous results by systematically characterizing the most promising compositions within the Ni–Nb–(Ta)–(P) alloy families. Emphasis is placed on their thermodynamic properties, kinetic behavior, and crystallization processes, which are essential for a fundamental understanding of the glass formation process.

* Corresponding author.
E-mail address: lucas.ruschel@uni-saarland.de (L.M. Ruschel).

https://doi.org/10.1016/j.actamat.2026.121918
Received 3 August 2025; Received in revised form 5 December 2025; Accepted 9 January 2026
Available online 9 January 2026

Thermodynamics determines the stability of the supercooled liquid and the driving force for crystallization. Kinetics governs the atomic mobility and the time scales over which structural arrest occurs. Crystallization studies reveal the transformation pathways, providing insight into the thermal stability and structural evolution of the alloys. Furthermore, information on crystallization enables the identification of competing phases that emerge during cooling. This knowledge enables the development of strategies to suppress these phases and further improve the GFA of Ni–Nb-based alloys. Moreover, crystallization data obtained during heating are also important for modern processing techniques such as selective laser melting, where heat-affected zones may cause previously solidified layers to crystallize over time. Understanding the thermal stability and crystallization pathways is therefore crucial for both further alloy optimization and the expansion of processing routes for Ni–Nb-based BMGs. By combining thermodynamic, kinetic, and crystallization insights, the present work provides a coherent framework for understanding the mechanisms that govern the enhanced GFA of Ni–Nb–(Ta)–P glass-forming alloys.

2. Experimental procedure

2.1. Sample production and characterization

Alloys of the compositions $Ni_{62}Nb_{38}$, $Ni_{59.2}Nb_{38.8}P_2$, and $Ni_{59.2}Nb_{33.8}Ta_5P_2$ were synthesized from the high-purity elements Ni (99.95 wt%), Nb (99.9 wt%), Ta (99.95 wt%) and P (99.999 wt%). To incorporate P into the system, a Ni_3P (Ni - 75 at%, P - 25 at%) pre-alloy was first produced via inductive melting in a quartz tube under a high-purity argon atmosphere. Further details of the pre-alloy production can be found in Ref. [13]. Based on the target compositions, the raw elements were alloyed with the appropriate amount of pre-alloy and the elements in an electric arc furnace under a Ti-gettered high-purity argon atmosphere (99.999% purity). Homogeneous element distribution was ensured by flipping and remelting the ingots at least five times. The master alloys were further processed via suction casting, with dimensions well below the critical casting thickness of each alloy, ensuring the production of amorphous specimens. The sample dimensions are specified in the description of each method. Their glassy structure was verified by conventional X-ray diffraction and differential scanning calorimetry.

2.2. Differential scanning calorimetry

Thermal analysis was performed using a power-compensated PerkinElmer DSC 8000 under a constant flow of high-purity argon gas (Ar 6.0) using copper pans. The isobaric specific heat capacity was determined using a step-method with a sapphire standard as a reference, following the approach reported in Refs. [17,18]. A heating rate of $0.333\,\mathrm{K\,s^{-1}}$ was applied, with temperature steps of $\Delta T = 10\,\mathrm{K}$ and equilibration times of $\Delta t = 120\,\mathrm{s}$. In the first measurement run, the heat capacity of the glass and supercooled liquid (SCL) was recorded up to crystallization. In a second measurement, the heat capacity of the crystalline phase was determined. To obtain isothermal heat-capacity data at multiple absolute temperatures, four measurements with an identical step protocol ($\Delta T = 10$ K, $\Delta t = 120$ s) were performed on fresh samples, while only the starting temperature was shifted by 2.5 K. This approach increases the effective sampling density, which is particularly important in the supercooled liquid region (SCLR). The experimental data are then modeled using the 'Kubaschewski' equations to describe the specific heat capacity of the liquid (c_p^l) and crystalline state (c_p^x) as follows:

$$c_p^l(T) = 3R + aT + bT^{-2}, \tag{1}$$

and

$$c_p^x(T) = 3R + cT + dT^2, \tag{2}$$

with the universal gas constant R (= $8.314\,\mathrm{J\,mol^{-1}\,K^{-1}}$) and fitting parameters a, b, c and d.

2.3. Low-temperature viscosity

The low-temperature viscosity near the glass transition was measured using a 3-point beam bending setup with a Netzsch TMA 402 F3 Hyperion thermomechanical analyzer (TMA). Rectangular beam-shaped specimens, with a width of 2 mm and thicknesses between 0.3 and 0.6 mm to ensure a proper signal-to-noise ratio, were centrally loaded with a constant force of 0.1 N. The midpoint deflection was continuously monitored throughout the experiment, with the deflection rate ν being inversely proportional to viscosity, as described by [19]:

$$\eta = -\frac{gL^3}{144 I_c \nu}\left[M + \frac{\rho A L}{1.6}\right], \tag{3}$$

with g being the gravitational constant, L being the support span (in this work: $L = 10$ mm), I_c being the cross-sectional moment of inertia, M the loading mass, ρ the density, and A the cross-sectional area. Theoretical densities, calculated from the molar masses and alloy compositions under the assumption of ideal mixing (i.e., without excess volume), were used to determine the low-temperature viscosity. Fig. A.1 in the appendix demonstrates that the viscosity obtained from the TMA method is only weakly affected by the assumed density, confirming that the use of theoretical density values is sufficient.

Two techniques were used to determine the viscosity in the deeply SCL. First, continuous heating experiments at $0.333\,\mathrm{K\,s^{-1}}$ up to the onset of crystallization, allowing for the characterization of viscosity within the SCLR. Additionally, isothermal measurements below the kinetic glass transition temperature ($T_g^* = 10^{12}$ Pa s) were performed to determine the equilibrium viscosity at long time scales. For these experiments, samples were heated at $0.333\,\mathrm{K\,s^{-1}}$ to the target temperature and held isothermally until a constant deflection rate was reached. The resulting viscosity data were fitted using the Kohlrausch-Williams-Watts (KWW) stretched exponential equation, describing the material's relaxation behavior, according to [20,21]:

$$\eta(t) = \eta_g + \eta_{eq-g}\left[1 - exp\left(-\left(\frac{t}{\tau}\right)^{\beta}\right)\right], \tag{4}$$

with η_g being the initial viscosity of the glass before relaxation, η_{eq-g} being the viscosity increase during relaxation into the equilibrium liquid on long time scales, τ being the relaxation time and β being the stretching exponent. The viscosity of the equilibrium liquid is obtained via $\eta_{eq} = \eta_g + \eta_{eq-g}$.

2.4. High-temperature viscosity

Container-less electromagnetic levitation of a metallic droplet in microgravity (TEMPUS: "Tiegelfreies Elektromagnetisches Prozessieren unter Schwerelosigkeit") is an ideal method to determine the high temperature viscosity of reactive metallic melts using a high-frequency alternating magnetic field [22]. The advantage of this method is that the melt does not come into contact with a crucible, thus avoiding contamination of the material. These electromagnetic levitation experiments can also be conducted on earth, however, the microgravity condition has several advantages. Stable sample positioning can be achieved with significantly lower field strengths, since the gravitational forces are much smaller (~zero gravity) compared to terrestrial conditions. This allows the electromagnetic Lorentz forces to be used only for sample positioning rather than for levitation. In addition, the reduced field strength minimizes the turbulent flow caused by induced convection as well as the absence of Earth's gravitational field allows the droplet to be nearly spherical, which has a significant effect on the accuracy of the obtained viscosity [23].

The experiments are carried out in an inert Ar-atmosphere with a reduced gravity time window of around 22 s for each parabola. The spherical sample (6.5 mm in diameter), which was previously produced by suction casting, was preheated to 1200 K prior to each parabola and then heated with a voltage of 10 V to a maximum temperature

of ~1800 K upon entering the microgravity phase. The heating coil was switched off and the droplet was compressed during He-quenching by two excitation pulses to trigger an oscillation decay behavior. A total of ten parabolas were performed, differing only in the maximum temperature. In this way, a larger temperature range is covered, as the onset of the excitation pulses is time-controlled so that they always occur at different temperatures. The whole process was recorded with a high speed camera with a frame rate of 400 fps and the movie was further processed using a digital image software to obtain the radius change of the droplet in X- and Y-direction as a function of time. The decay over time as a result of internal friction of the sample can be expressed with a cosine-damped function [23]:

$$r(t) = r_0 + A\ cos(\omega t)\ exp(-\Gamma t), \tag{5}$$

with the radius change as a function of time $r(t)$, the quiescent radius of the droplet r_0, the oscillation amplitude A, the angular frequency ω, and the damping constant Γ. Details can be found in Fig. A.3 of the Appendix.

In the context of microgravity conditions, where turbulence, surface layers and external forces are largely excluded, viscous damping becomes the primary dissipation mechanism. Then the damping constant is directly proportional to the viscosity η, given by [24]:

$$\eta(T) = \frac{3m\Gamma}{20r_0\pi}, \tag{6}$$

where m is the sample mass, Γ the damping constant and r_0 the quiescent radius. The radius r_0 was determined from the sample mass and the theoretical density based on ideal mixing. In Fig. A.1 of the appendix, it is demonstrated that using a theoretical density is sufficient and has a negligible influence on the determined viscosity.

To ensure that the extracted damping originates exclusively from viscous dissipation, the linearity of the oscillations was verified following the established criteria proposed by Lohöfer [25,26] and Wunderlich & Mohr [27]. Only stable, symmetric single-mode oscillations were analyzed, and the damping rate was found to be independent of the oscillation amplitude. This confirms that nonlinear, turbulence-related, or surface-induced damping contributions are negligible. Together with the absence of coupled modes and the fulfillment of the Rayleigh–Lamb conditions, this ensures that the oscillation decay is governed primarily by viscous dissipation. Additionally, the frequency-domain representation of the oscillation signal was examined, and only oscillations whose Fast Fourier Transform spectra exhibited a single resonance peak were considered for viscosity evaluation, as shown in Fig. A.2 of the Appendix.

Since the TEMPUS experiments are performed during continuous cooling, the viscosity values obtained represent an average over a specific temperature range (typically about 25–50 K, see Appendix Fig. A.4). More details on the oscillating drop technique can be found in Refs. [22–24]

2.5. Modeling of viscosity

The viscosities in the liquid can be described with different models. A commonly used model to describe the change of viscosity $\eta(T)$ as a function of temperature and quantify the fragility is the Vogel–Fulcher–Tamman (VFT) relation [28–31]:

$$\eta(T) = \eta_0 exp\left(\frac{D^* T_0}{T - T_0}\right), \tag{7}$$

with D^* being the fragility parameter, which describes the temperature dependence of viscosity, T_0 being the VFT-temperature at which the viscosity diverges to infinity and η_0 being the pre-exponential factor, which describes the viscosity at infinite temperature. For each composition, η_0 was estimated according to the relation $\eta_0 = N_A h/V_m$ (see Table 4, where N_A is Avogadro's constant, h is Planck's constant and V_m is the molar volume [17,32].

Table 1
Details of the experimental setup used for the high-energy X-ray diffraction experiments at PETRA III of DESY.

Parameter	Unit	P21.1	P21.1	P21.2
Experiment	–	Furnace	Levitation	Levitation
Energy	keV	100	101.6	97
Wavelength	Å	0.12398	0.12203	0.12782
Beam size	mm^2	0.5 × 0.5	1 × 1	1 × 1
Detector	–	Perkin Elmer XRD1621 CsI	Perkin Elmer XRD1621 CsI	VAREX XRD4343CT
Resolution	pixels	2048 × 2048	2048 × 2048	2880 × 2880
Pixel size	µm	200	200	150

Additionally, the extended MYEGA (Mauro, Yue, Ellison, Gupta, Allan) relation, which allows to describe the change in viscosity from an initially fragile into a strong liquid, enables an improved extrapolation of viscosity based on:

$$log\ \eta(T) = log\ \eta_0 + \left[T\left(W_1 exp\left(-\frac{C_1}{T}\right) + W_2 exp\left(-\frac{C_2}{T}\right)\right)\right]^{-1} \tag{8}$$

with η_0 representing the theoretical viscosity at infinite temperature and C_1 and C_2 representing two different onsets, at which structural constraints cause a floppy-to-rigid transition. Both contributions are weighted by W_1 and W_2. For more information on the physical background and the detailed derivation of this equation, the reader is referred to the original papers [33,34].

2.6. High-energy synchrotron X-ray diffraction

In-situ high energy X-ray diffraction (HE-XRD) experiments were performed to study the structure of the high temperature liquid in two separate beamtimes at the beamline facility P21.1 and P21.2 of PETRA III of the 'Deutsches Elektronensynchrotron' (DESY) in Hamburg using an electrostatic levitation (ESL) device. Spherical droplets weighing about 100 mg were levitated in an ultra-high vacuum ($<10^{-6}$ mbar) and heated by two infrared lasers with a power of 75 W (λ = 808 nm). The temperature was recorded with a pyrometer, which was calibrated to the melting point of the respective composition during post-experiment analysis. The HE-XRD diffraction patterns were recorded continuously with an acquisition time of 1 s for each diffraction pattern.

Additionally, furnace heating experiments were conducted at P21.1 to study the structural evolution of the glassy state up to the supercooled liquid using a Linkam TS1500 furnace. The initial temperature protocol was performed from room temperature to 773 K with a heating rate of 1 Ks^{-1} and from there continued up to crystallization using a rate of 0.333 Ks^{-1}. The change in heating rate was applied well below the glass transition, i.e., in a temperature range where no structural relaxation or other structural changes occur. The initial higher heating rate was chosen to reduce measurement time, as structural changes in this temperature range are limited to thermal expansion. The reduced heating rate at temperatures close to the glass transition was chosen to obtain better temperature resolution of the glass transition and SCLR. The acquisition time of each recorded diffraction pattern was set to 5 s. Table 1 summarizes the experimental details of each beamtime.

The acquired two-dimensional images were azimuthally integrated using the PyFAI program [35]. After applying background scattering corrections and accounting for multiple scattering, fluorescence, and Compton scattering with PDFgetX2 [36], the corrected intensity function $I(Q)$ was obtained.

3. Results

3.1. Thermodynamics of Ni–Nb-(Ta)-P

The thermodynamic functions are crucial parameters to understand the GFA of a system, in particular the driving force for crystallization

ΔG_{l-x}. To obtain ΔG_{l-x}, the Gibbs free energy curves are required, which can be fundamentally obtained from the specific heat capacity measurement of the liquid and crystalline state $c_p^l(T)$ and $c_p^x(T)$, respectively. While the $c_p^x(T)$ can be determined relatively easily in a low-temperature power-compensated DSC with high accuracy via the step-method, the available DSC sensor for the high-temperature DSC was not sufficiently accurate for $c_p^l(T)$ measurements with a high precision. This is connected to various problems, that are encountered at temperatures exceeding approximately 1273 K. First, the sample starts to emit significant amounts of thermal radiation, which is not completely absorbed by the DSC sensor, leading to an incorrect heat flow. Secondly, the high melting temperature of Ni–Nb alloys (about 1445 K) require special handling and preparation of the crucibles to avoid reactions and thus contamination. Therefore, all crucible were coated with an Y_2O_3 layer to avoid any reaction of the sample with the crucible material. However, as the coating was applied manually, there is potential variation in the mass of the individual crucibles of maximum ±10 mg, thereby affecting the accuracy of the measurements. This is unproblematic for standard scans, since the changes in the enthalpy (e.g. ΔH_x and ΔH_l) are relatively large, however in the case of high-precision $c_p^l(T)$ measurements, this becomes relevant as the changes with temperature are relatively small. Moreover, the melt is highly reactive at high temperatures around T_l, resulting in sample degradation due to oxidation, irrespective of the constant argon flow throughout the measurement. This is particularly pronounced when the melt is maintained for an extended period in the high-temperature equilibrium liquid, which is necessary for conducting $c_p^l(T)$ measurements.

To overcome this issue, an alternative approach based on the simplification of the Kubaschewski equations was employed. It is known that the region between the onset of crystallization T_x and the liquidus temperature T_l corresponds to the difference between the enthalpy of fusion ΔH_f and the enthalpy difference ΔH_{l-x}. In this context, the latter corresponds to the measured crystallization enthalpy release ΔH_x upon reheating of an amorphous sample, leading to the following relation:

$$\Delta H_f - \Delta H_x = \int_{T_x}^{T_l} \Delta c_p^{l-x}(T')dT', \tag{9}$$

which describes the area under the Δc_p^{l-x} curved between T_x and T_l (see Fig. 1).

By separating the integral of the specific heat capacity difference into individual terms, the integral of the specific heat capacity of the liquid $\int c_p^l(T')dT'$ can be described by the enthalpy of fusion ΔH_f, the crystallization enthalpy ΔH_x and the integral $\int c_p^x(T')dT'$, which are properties easily accessible by calorimetric experiments. The determination of $c_p^x(T)$, in particular, is not an issue compared to $c_p^l(T)$, as no severe sample deterioration or crucible reactions occur within the applied temperature range (from room temperature up to 973 K), as the solid state is distinctly less reactive. This results in:

$$\underbrace{\Delta H_f - \Delta H_x + \int_{T_x}^{T_l} c_p^x(T')dT'}_{=A} = \int_{T_x}^{T_l} c_p^l(T')dT'. \tag{10}$$

The left-hand side of the equation is abbreviated in the following with the constant A, since ΔH_f, ΔH_x are constant as well as $\int c_p^x(T')dT'$ within the specified temperature interval T_x to T_l. Now, $c_p^l(T)$, described by the Kubaschewski Eq. (1), can be inserted into Eq. (10). Solving the integral and transforming it according to the constant b results in:

$$\begin{aligned} A &= \int_{T_x}^{T_l} (3R + aT' + bT'^{-2})dT' \\ \Leftrightarrow b &= \frac{A - 3R(T_l - T_x) - \frac{a}{2}(T_l^2 - T_x^2)}{T_x^{-1} - T_l^{-1}}, \end{aligned} \tag{11}$$

with R being the universal gas constant (=8.314 J mol^{-1} K^{-1}), and a being a fitting parameter.

This reduction of the initial Kubaschewski equation containing two fitting parameter (a and b) to a single parameter equation (only a, as b can be described as a function of a according to Eq. (11)) allows a proper determination of $c_p^l(T)$ when the specific heat capacity of the SCL in the vicinity of the glass transition is available. However, it should be mentioned that the accuracy of this method is limited, as the fit is based on a few data points in the SCL as well as the determined values of ΔH_x and ΔH_f. No data for ΔH_x over the full temperature range from T_x to T_l are available in the literature for direct comparison. However, the measured values of ΔH_f (approximately 13.6–15.3 kJ g-atom^{-1}, see Table 3) are in close agreement with those reported for similar Ni–Nb alloys in Ref. [37] (13.6 kJ g-atom^{-1}). Since ΔH_x and ΔH_f are determined from the same DSC measurement, the reliability of ΔH_f indicates that the determined ΔH_x values are likewise accurate. Nevertheless, the specific heat capacity fit of the liquid should be

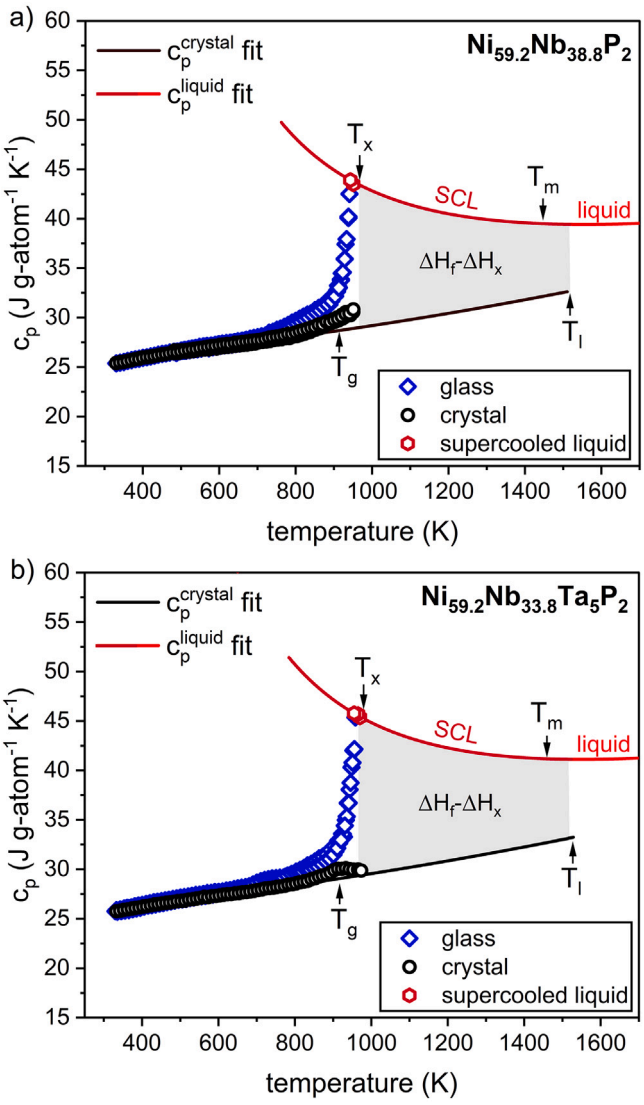

Fig. 1. Molar heat capacity of the crystalline, glassy, and liquid states, represented by black, blue, and dark-red symbols, respectively, for the best glass-forming alloys (a) $Ni_{59.2}Nb_{38.8}P_2$ and (b) $Ni_{59.2}Nb_{33.8}Ta_5P_2$ of their respective system. The corresponding fits $c_p^l(T)$ and $c_p^x(T)$ are obtained according to Eqs. (1) and (2), respectively. As no data in the equilibrium state were available, Eq. (1) was simplified by pinning the fit to the enthalpy of fusion ΔH_f and crystallization enthalpy ΔH_x, as indicated by the gray area. Additionally, the characteristic temperatures T_g (glass transition), T_x (onset of crystallization), T_m (melting temperature), and T_l (liquidus temperature) are indicated. (For interpretation of the references to color in this figure legend, the reader is referred to the web version of this article.)

Table 2
Fitting parameters of the Kubaschewski Eq. (1) and (2) for the best glass-forming alloy $Ni_{59.2}Nb_{38.8}P_2$ and $Ni_{59.2}Nb_{33.8}Ta_5P_2$ of the ternary and quaternary system, respectively. *a* and *b* correspond to the fitting parameters describing $c_p^l(T)$, while *c* and *d* are required for $c_p^x(T)$.

Alloy	*a* [×10^{-3}] (J g-atom^{-1} K^{-2})	*b* [×10^{7}] (J g-atom^{-1} K)	*c* [×10^{-3}] (J g-atom^{-1} K^{-2})	*d* [×10^{-6}] (J g-atom^{-1} K^{-3})
$Ni_{59.2}Nb_{38.8}P_2$	6.2100	1.1665	2.6400	1.6268
$Ni_{59.2}Nb_{33.8}Ta_5P_2$	6.9700	1.2934	3.1600	1.4895

treated with caution due to the aforementioned constraints, which will be critically discussed later on.

Molar heat capacity measurements were successfully conducted for $Ni_{59.2}Nb_{38.8}P_2$ and $Ni_{59.2}Nb_{33.8}$-Ta_5P_2 (Fig. 1). The analysis of the binary alloy $Ni_{62}Nb_{38}$ could not be performed due to the limited stability of the SCLR and rapid crystallization. Given the isothermal nature of the measurement technique and the relatively narrow SCLR of the studied alloys, it is particularly challenging to obtain data points in the SCL. Accordingly, the starting temperature was shifted by 2.5 K for each measurement (4 measurements for each composition) to cover a broader temperature range and improve data collection within the SCL. Fig. 1 depicts the specific heat capacity data points for the glass and glass transition region (blue symbols), a few data points in the SCLR (dark red symbols), and the crystalline state (black symbols) of a) $Ni_{59.2}Nb_{38.8}P_2$ and b) $Ni_{59.2}Nb_{33.8}Ta_5P_2$. The most relevant characteristic temperatures are indicated as T_g, T_x, T_m, and T_l. It should be noted that T_g and T_x correspond to the values obtained with a heating rate of 0.333 Ks^{-1}, while T_m and T_l are independent of the rate. The black curve represents the $c_p^x(T)$ fit according to the Kubaschewski Eq. (2), while the dark red curve represents the fit of the liquid state according to Eq. (1) and the 'pinning method' described above. The resulting fitting parameters are summarized in Table 2.

The Gibbs free energy, enthalpy, and entropy difference between the (supercooled) liquid and the crystalline state is calculated based on the previously determined fit functions $c_p^x(T)$ and $c_p^l(T)$. The results of both alloys are presented in Fig. 2 on the left for $Ni_{59.2}Nb_{38.8}P_2$ and on the right for $Ni_{59.2}Nb_{33.8}Ta_5P_2$. The enthalpy of crystallization ΔH_x as well as enthalpy of fusion ΔH_f are indicated at the crystallization temperature T_x and liquidus temperature T_l, indicating an overall higher enthalpic state for the Ta-containing alloy. Nevertheless, the two alloys exhibit comparable behavior, which is to be expected given their similar composition. Below the fictive temperature T_f in the vitrified state, the enthalpy difference remains approximately constant (neglecting relaxation processes) with a certain residual enthalpy that has been frozen-in. The fictive temperature, i.e. the freezing temperature of cooling, was determined for a 5 and 6 mm amorphous rod (critical casting size of Ni–Nb–P and Ni–Nb–Ta–P, respectively) according to the Moynihan method [38]. As can be observed in Fig. 2a and d, the enthalpy curve of the liquid state continues below T_f, which represents the SCL on long time scales. Given that a system is always driven to reduce its free energy, the system will relax towards the more favorable state of the supercooled liquid. This relaxation process is typically observed at elevated temperatures in the vicinity of T_g due to an increased atomic mobility, such as during a scan measurement or isothermal annealing.

An analogous course demonstrates the entropy difference ΔS_{l-x} for both alloys in Fig. 2b and e. In general, the entropy difference is decreasing due to the structural ordering towards a more pronounced SRO and MRO with decreasing temperature until a well-defined structure is frozen-in at the fictive temperature. The temperature at which the entropy difference of the SCL intersects with that of the crystal ($\Delta S_{l-x} = 0$) represents the Kauzmann temperature, T_K. From a thermodynamic perspective, T_K represents the lowest temperature at which glass transition must occur, as the entropy of a 'disordered' liquid cannot be lower than that of the corresponding ordered crystal [39].

The Gibbs free energy difference ΔG_{l-x} can be determined from the previously obtained enthalpy ΔH_{l-x} and entropy ΔS_{l-x} difference

Table 3
The fictive temperature T_f was determined by the Moynihan method. The crystallization enthalpy ΔH_x, enthalpy of fusion ΔH_f, entropy of fusion ΔS_f are determined from DSC measurements. The Gibbs free energy difference ΔG_{l-x} is calculated from the molar heat capacity functions of the liquid and the crystal mixture. $\Delta G_{l-x}^{Turnbull}$ corresponds to the driving force according to the Turnbull approximation.

		Alloy	
Parameter	Unit	$Ni_{59.2}Nb_{38.8}P_2$	$Ni_{59.2}Nb_{33.8}Ta_5P_2$
T_f	(K)	949	961
ΔH_x	(kJ g-atom^{-1})	8.06	9.19
ΔH_f	(kJ g-atom^{-1})	13.56	15.27
ΔS_f	(J g-atom^{-1} K^{-1})	8.93	10.00
ΔG_{l-x}	(kJ g-atom^{-1})	3.95	4.45
$\Delta G_{l-x}^{Turnbull}$	(kJ g-atom^{-1})	5.09	5.66

curves, providing insight in the thermodynamic driving force for crystallization. For $Ni_{59.2}Nb_{38.8}P_2$, ΔG_{l-x} at the fictive temperature results in a value of 3.95 kJ g-atom^{-1}, while it yields 4.45 kJ g-atom^{-1} for $Ni_{59.2}Nb_{33.8}Ta_5P_2$. Alternatively, the Gibbs free energy difference can be approximated according to Turnbull from the knowledge of the enthalpy of fusion ΔH_f and the liquidus temperature T_l, resulting for $Ni_{59.2}Nb_{38.8}P_2$ in a value of 5.09 kJ g-atom^{-1} and for $Ni_{59.2}Nb_{33.8}Ta_5P_2$ in a value of 5.66 kJ g-atom^{-1}. The Turnbull approximation is also given as dotted line in Fig. 2. To further assess the reliability of this approximation, literature values of ΔH_f, T_L [37], and T_g [40] for binary Ni–Nb were used to estimate the driving force for crystallization via the Turnbull approximation, yielding a value of $\Delta G_{l-x}^{Turnbull} = 5.15$ kJ g-atom^{-1}, which closely matches the values determined in this work for the Ni–Nb–P and Ni–Nb–Ta–P alloys. This comparison provides valuable insight into the magnitude of the driving force and supports the reliability of the pinning method described above. It can be seen that the approximation yields high values in the driving force for crystallization $\Delta G_{l-x}^{Turnbull}$, resulting from the high entropy of fusion relative to other glass-forming alloys. In contrast, ΔG_{l-x} derived from the specific heat capacity data is lower and rather represents the lower boundary for the driving force for crystallization, as it additionally accounts for the actual temperature dependence of the liquid heat capacity. Accordingly, regardless of the method used, Ni–Nb-based alloys exhibit a comparatively high thermodynamic driving force for crystallization relative to many other metallic glass formers [4,41,42].

3.2. Low- and high-temperature viscosity and fragility

The viscosity and its temperature dependence in the deeply SCL at low-temperature is assessed for a) $Ni_{62}Nb_{38}$, b) $Ni_{59.2}Nb_{38.8}P_2$ and c) $Ni_{59.2}Nb_{33.8}Ta_5P_2$, as can be seen in Fig. 3. The left inset at the top of each of the graphs presents a selection of isothermal TMA measurements, which demonstrate the relaxation process from the glassy state (for isothermal temperatures below T_g) into the SCLR. The data can be fitted with a KWW function (dashed–dotted lines), providing information about viscosity on long time scales at the respective isothermal temperatures. The equilibrium viscosities obtained are represented by the blue symbols in the graphs. The abrupt rise in viscosity at isothermal temperatures close to T_g is attributable to primary crystallization. A similar rise in viscosity is also observed in

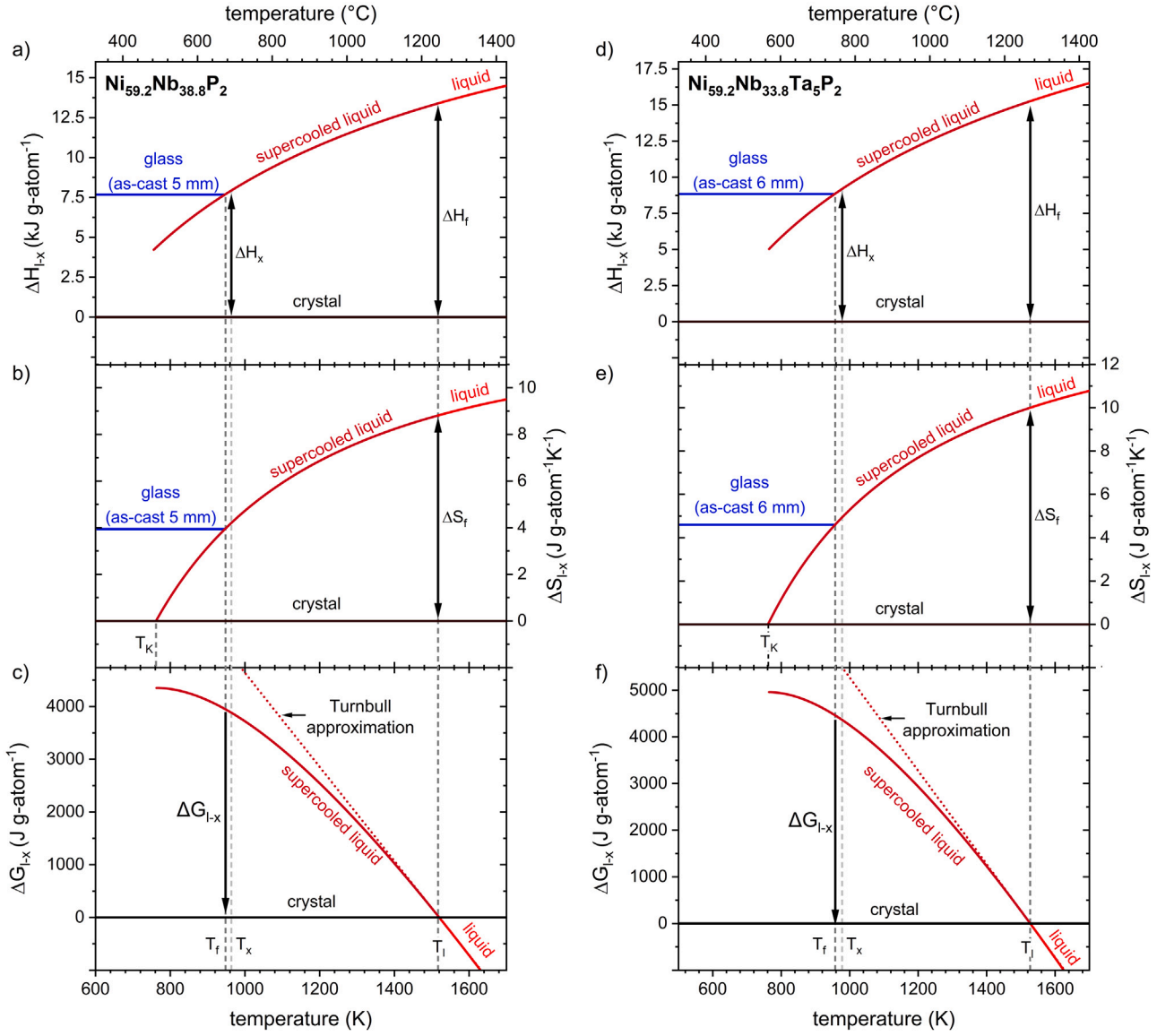

Fig. 2. The thermodynamic functions, including the difference in enthalpy (ΔH_{l-x}), entropy (ΔS_{l-x}), and Gibbs free energy (ΔG_{l-x}) of the SCL with respect to the crystalline state, are presented in (a), (b), and (c) for $Ni_{59.2}Nb_{38.8}P_2$ and in d), e), and f) for $Ni_{59.2}Nb_{33.8}Ta_5P_2$. The indicated parameters represent the Kauzmann temperature, T_K, along with T_g, T_x, and T_l, which represent the glass transition temperature, the crystallization temperature, and the liquidus temperature, respectively. ΔH_x corresponds to the crystallization enthalpy and ΔH_f to the enthalpy of fusion. The horizontal blue line represents the respective glassy state of the critical casting size with a fictive temperature of T_f = 948 K for $Ni_{59.2}Nb_{38.8}P_2$ and T_f = 958 K for $Ni_{59.2}Nb_{33.8}Ta_5P_2$. (For interpretation of the references to color in this figure legend, the reader is referred to the web version of this article.)

the TMA scan, closely aligning with the onset of crystallization in the DSC scan, as shown in the lower panel to serve as an orientation.

The TMA scan can be divided into three distinct regions. In the low-temperature region (below T_g), the viscosity remains relatively constant and exhibits considerable scatter, as the sample does not undergo significant deflection in the glassy state. As the glass transition region is approached, the system devitrifies and enters the SCLR. Here, the viscosity declines continuously with increasing temperature (quasi-Arrhenius or VFT-like behavior) until the liquid crystallizes. When crystallizing, the alloy starts to behave like a solid, which is reflected in the sudden rise in apparent viscosity. Interestingly, an anomalous increase in viscosity is observed in $Ni_{59.2}Nb_{33.8}Ta_5P_2$ prior to crystallization (red circle in Fig. 3c) and may be related to a phase separation in the SCL, as often reported in glass-forming liquids [43–46]. Nevertheless, the fragility parameter D^* and thus the kinetic fragility at low temperatures can still be determined by fitting the SCLR of the scan measurements in combination with the equilibrium viscosity at long timescales determined from sub-T_g relaxation experiments with the VFT equation.

The obtained fragility parameters for all studied Ni–Nb alloys, along with the corresponding fitting parameters, are summarized in Table 4. The binary base alloy shows the most fragile behavior, with a fragility parameter D^* of 13.9, increasing to 17.2 for the P-containing Ni–Nb–P alloy and reaching 18.3 for the quaternary Ni–Nb–Ta–P alloy. This increase with the increased number of alloying elements is expected, as the reduction of atomic mobility was the primary objective of the alloy development conducted in Ref. [13]. Interestingly, binary $Ni_{62}Nb_{38}$ already exhibits a relatively strong behavior, which is unusual for binary alloys, as the fragility of those is expected to be rather in the range of monoatomic liquids with a $D^* \approx 2$ or slightly higher [4]. For this reason, most metallic glasses are typically multi-component alloys with four to five components of different sizes to achieve stronger liquid fragility [47]. Binary bulk glass-forming alloys, such as Cu–Zr and Ni–Nb, generally appear to be an exception, as they exhibit reduced

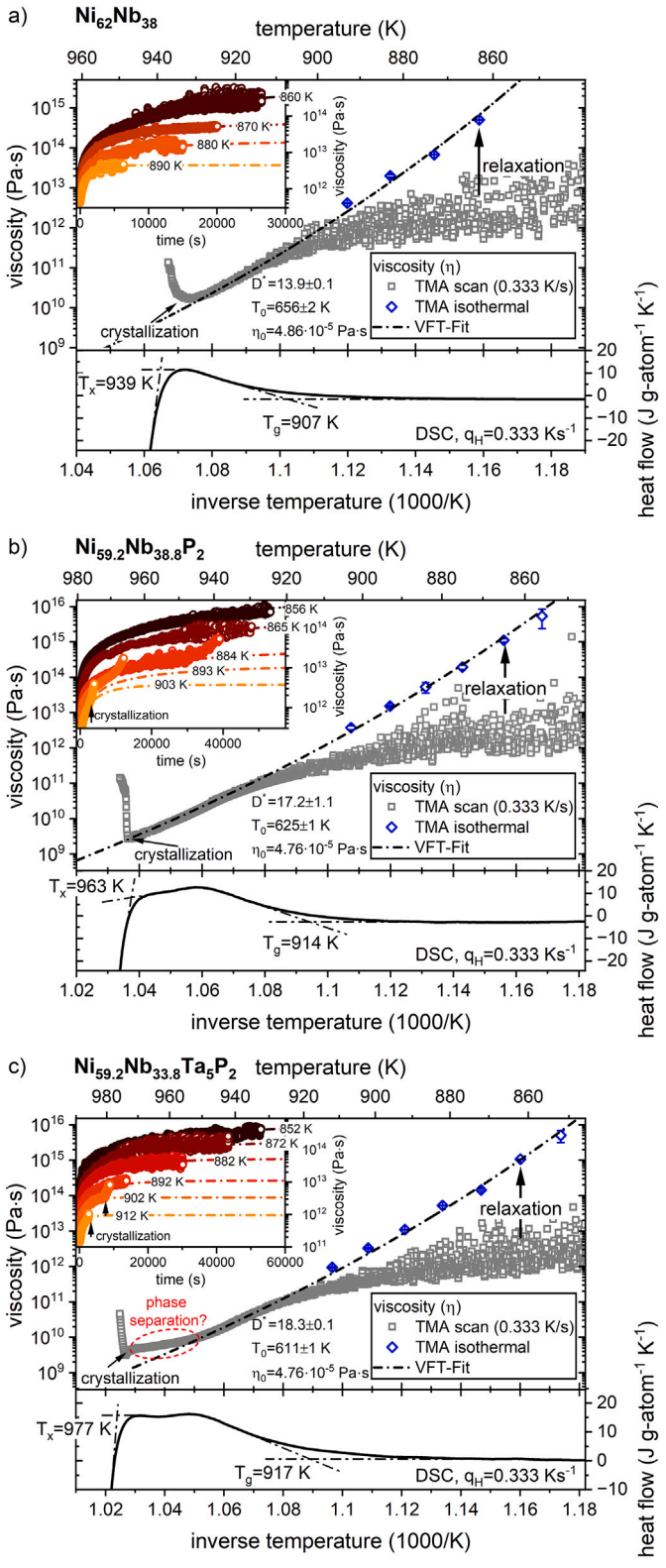

Fig. 3. Low temperature viscosity of (a) $Ni_{62}Nb_{38}$, (b) $Ni_{59.2}Nb_{38.8}P_2$ and (c) $Ni_{59.2}Nb_{33.8}Ta_5P_2$. The plot is divided into three parts. The top left inset shows the isothermal viscosity measurements below the glass transition, fitted by KWW fits to describe the relaxation process from glassy state to the equilibrium liquid on long timescales. The equilibrium viscosities are plotted as a function of inverse temperature along a TMA scan measurement, which are both fitted by the VFT equation (black dashed–dotted line). The lower panel shows the DSC scan of the respective alloys and serves as orientation.

atomic mobility even in their binary state. This is reflected in their relatively low kinetic-fragility parameter m (=slope of viscosity at T_g^*), with Cu–Zr showing an m-fragility of 62 [48], comparable to that of Ni–Nb with $m = 60$ (see Table 4). The trend to a progressively stronger liquid is further evident in the thermal stability ΔT_x of the alloys, which increases from 32 K for $Ni_{62}Nb_{38}$, to 49 K for $Ni_{59.2}Nb_{38.8}P_2$, and 60 K for $Ni_{59.2}Nb_{33.8}Ta_5P_2$ and has been observed for earlier Ni–Nb and Zr-based BMGs [49]. A more stable SCLR typically indicates higher viscosities and thus higher resistance to crystallization (i.e. lower atomic mobility), which is in accordance with the observed increase in GFA when P and Ta is introduced.

Fig. 4a compares the high-temperature viscosity of $Ni_{62}Nb_{38}$ with $Ni_{59.2}Nb_{38.8}P_2$. The binary alloy was measured by Mauro et al. using an electrostatic levitator as reported in Ref. [50], while the ternary composition was measured during a parabolic flight campaign using electromagnetic levitation. In the latter, the sample was rapidly heated to the equilibrium liquid state by a heating coil, followed by free cooling. During this cycle, two excitation pulses induced damped oscillations, and their decay correlates directly with viscosity according to Eq. (6). The uncertainty in viscosity shown in Fig. 4 corresponds to the mean value of the oscillation in the X- and Y-directions, both fitted with a damped cosine function. The temperature error is a consequence of the continuous cooling nature of the experiment. The measured viscosities above the liquidus temperature (gray dashed line) were in the range of 30 to 40 mPa·s, which is similar to the values obtained by Mauro et al. for binary Ni–Nb [50]. When supercooled below the liquidus temperature, the viscosity increases quickly to a range of 60 to 80 mPa·s. For the binary alloy, even lower temperatures and correspondingly higher viscosities could be measured, as ground-based experiments are not limited by time constraints. In contrast, the time window during the TEMPUS campaign was constrained to approximately 20–25 seconds per cycle, during which the sample was heated, cooled, and excited, limiting the extent of undercooling.

The high-temperature viscosity data were also fitted using a VFT-equation, with the fit pinned to the viscosity at the kinetic glass transition temperature T_g^* of each composition. This fitting revealed a relatively fragile behavior, with a kinetic fragility parameter D^*=6.6 for both the binary and ternary alloys. Such a discrepancy, where the low-temperature fragility exhibits a considerably stronger temperature dependence compared to the high-temperature liquid, is commonly observed in metallic glass-forming liquids and is documented well especially for Zr-based multi-component BMGs [51–53]. When comparing the data sets of both compositions, the viscosity and fragility appear similar at first glance, which is not surprising as only a small amount of P was added. Additionally, the atomic size of P is small and thus expected to be highly mobile at elevated temperatures. Nonetheless, when the temperature is normalized to the liquidus temperature to allow a proper comparison of both compositions, a difference between the binary and ternary alloy becomes apparent, as can be seen in Fig. 4b. The P-containing composition exhibits slightly higher viscosity at each normalized temperature, which is consistent with the findings at low-temperatures also indicating slower kinetics. However, these discrepancies should be interpreted with caution, given the small differences between both alloys as well as the uncertainties of the TEMPUS measurements. No data could be obtained for the quaternary $Ni_{59.2}Nb_{33.8}Ta_5P_2$ composition due to limited access to TEMPUS experiments. However, based on the similarity of the binary and ternary alloy, a similar viscosity behavior is expected for $Ni_{59.2}Nb_{33.8}Ta_5P_2$ at high temperature.

3.3. Crystallization behavior

Time–temperature-transformation (TTT) diagrams are measured to understand the influence of alloying elements on thermal stability, yielding insights how certain elements influence the atomic mobility

Table 4
Summary of the high and low-temperature VFT fitting parameters for the studied Ni–Nb alloys. While D^* and T_0 correspond to fitting parameters, η_0 was calculated based on the molar volume, as described in Ref. [4]. The kinetic glass transition temperature T_g^* and the fragility index m (slope at T_g^*) are derived from the VFT fit. The reported errors represent the fitting uncertainties.

		$Ni_{62}Nb_{38}$		$Ni_{59.2}Nb_{38.8}P_2$		$Ni_{59.2}Nb_{33.8}Ta_5P_2$
		high T	low T	high T	low T	low T
η_0	(10^{-5} Pas)	4.86	4.86	4.76	4.76	4.76
D^*	–	6.6 ± 0.1	13.9 ± 0.1	6.6 ± 0.1	17.2 ± 1.1	18.3 ± 0.1
T_0	(K)	765 ± 1	656 ± 2	775 ± 3	625 ± 1	611 ± 1
T_g^*	(K)	899	899	911	911	909
m	–	110	60	109	52	50

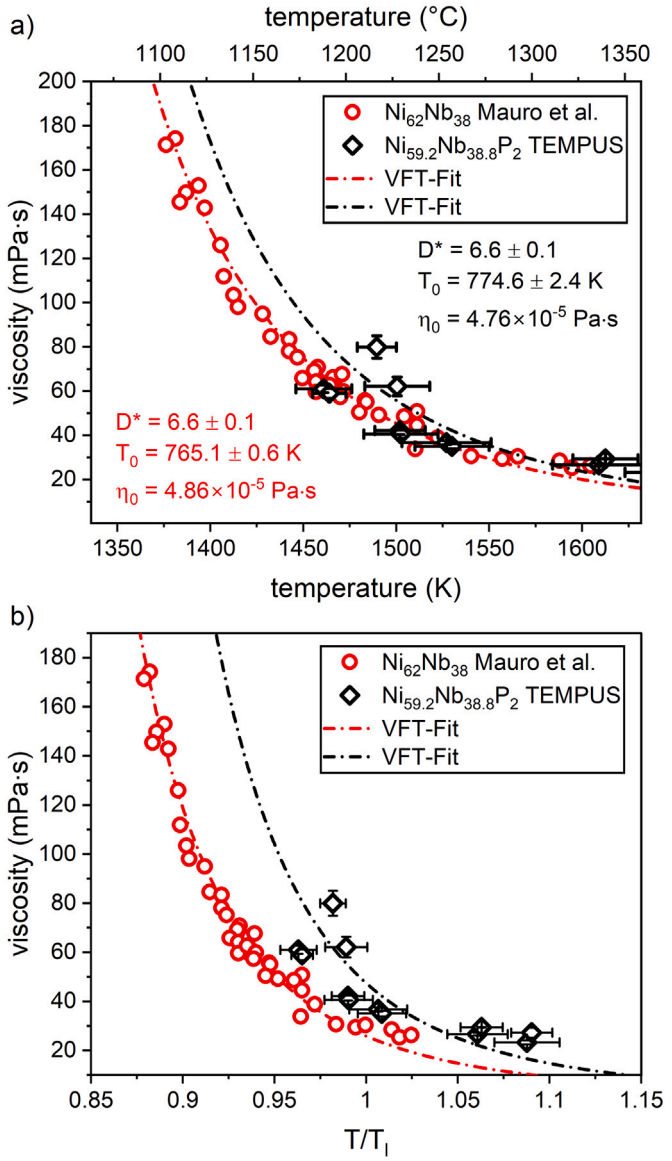

Fig. 4. (a) High temperature viscosity of $Ni_{62}Nb_{38}$ and $Ni_{59.2}Nb_{38.8}P_2$. The data for $Ni_{62}Nb_{38}$ were measured by ESL and are taken from Ref. [50], while those for $Ni_{59.2}Nb_{38.8}P_2$ were obtained from TEMPUS measurements during a parabolic flight campaign. b) Viscosity normalized to the liquidus temperature of each composition. The normalization reveals differences in viscosity, with $Ni_{59.2}Nb_{38.8}P_2$ showing higher values at each normalized temperature, indicating a kinetic slowdown due to P addition. The dashed–dotted lines represent the VFT-fit.

by retarding or accelerating crystallization. Fig. 5a presents isothermal measurements and the lower portion of the TTT diagrams for the best glass-forming composition of the respective binary, ternary, or quaternary system at various temperatures. The signature of the isothermal crystallization of $Ni_{62}Nb_{38}$ and $Ni_{59.2}Nb_{38.8}P_2$ exhibits a striking similarity, manifested in the form of a double crystallization peak. It is notable that the initial event is retarded by the minor addition of phosphorus, as evidenced by an increased overlap of both crystallization peaks for $Ni_{59.2}Nb_{38.8}P_2$. This destabilization of the crystallization process was already visible from DSC scans with a constant heating rate, where the onset for crystallization was pushed to a higher temperature with increasing P-content, as previously reported in Ref. [13]. Given that the initial crystallizing phase for $Ni_{62}Nb_{38}$ and $Ni_{59.2}Nb_{38.8}P_2$ corresponds to the metastable M-phase [54], which will be discussed in more detail further below, it appears that P destabilizes this phase. A complete destabilization occurs when Ta is incorporated, resulting in a single isothermal crystallization event, as shown for $Ni_{59.2}Nb_{33.8}Ta_5P_2$ in the lower panel of Fig. 5a.

The corresponding crystallization times, indicating 5 %, 50 % and 95 % crystallization, are given on the right in Fig. 5b. In order to demonstrate the effect of each alloying element more clearly, the temperature scale of the TTT diagrams has been normalized to the glass transition temperature. It can be observed that the thermal stability, or rather resistance against crystallization, increases from $Ni_{62}Nb_{38}$ over $Ni_{59.2}Nb_{38.8}P_2$ to $Ni_{59.2}Nb_{33.8}Ta_5P_2$. On such a scale, the low thermal stability of the binary $Ni_{62}Nb_{38}$ alloy is evident from the faster crystallization times at each normalized temperature T/T_g^{onset} when compared to the P- and Ta-containing alloys. Specifically, the latter exhibits the best combination between high GFA, thermal stability and resistance against crystallization within the Ni–Nb alloy family.

In-situ HE-XRD experiments upon heating from the glassy state are shown in Fig. 6. Each plot is divided into three parts showing on the left the evolution of all collected diffraction patterns as a function of temperature. The adjacent panel shows the DSC scan of this alloy with the same temperature scaling. The experiments were performed using the same heating rate of 0.333 Ks^{-1} as in the calorimetric experiments. This allows a direct comparison of the exothermic events in the DSC with the crystallizing phases. For a better overview and identification of the crystalline phases, a selection of diffraction patterns has been summarized in the right-hand figure, starting from the amorphous state up to the formation of the individual compounds. The color-coding from blue to red indicates the increasing temperature. The position of each diffraction pattern is additionally marked with a colored dot in the DSC scan.

Fig. 6 shows the evolution of the diffraction patterns upon heating for $Ni_{62}Nb_{38}$, $Ni_{59.2}Nb_{38.8}P_2$, and $Ni_{59.2}Nb_{33.8}Ta_5P_2$. When comparing $Ni_{62}Nb_{38}$ and $Ni_{59.2}Nb_{38.8}P_2$, both alloys look similar from their DSC signal, although the first exothermic event consists of two peaks for the $Ni_{62}Nb_{38}$ alloy and only one peak for the P-containing alloy. The addition of P appears to destabilize the first crystallizing phase, suggesting that this phase is no longer the primary phase upon heating in $Ni_{59.2}Nb_{38.8}P_2$. However, in-situ measurements provide a more nuanced picture. Once the atomic mobility is high enough for crystallization to set in, the amorphous halo begins to sharpen not only for

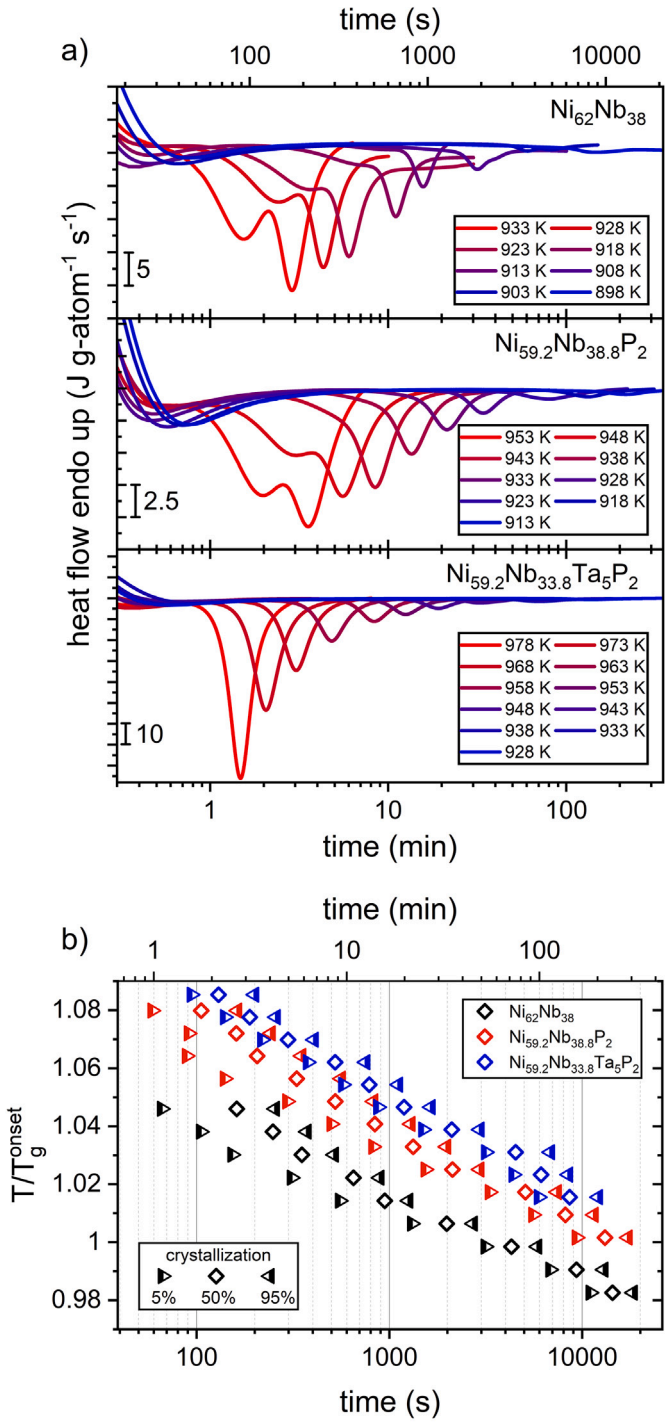

Fig. 5. Heat flow curves measured for different temperatures of (a) $Ni_{62}Nb_{38}$, $Ni_{59.2}Nb_{38.8}P_2$ and $Ni_{59.2}Nb_{33.8}Ta_5P_2$. The temperature of the respective measurement is color coded from the lowest temperature in blue to the highest in red. The isothermal TTT diagrams at low temperatures are obtained by integrating the exothermic crystallization peaks to calculate 5 %, 50 % and 95 % of the area, representing the amount of crystallization transformation. (b) TTT diagram normalized to T_g^{onset} for these alloys. (For interpretation of the references to color in this figure legend, the reader is referred to the web version of this article.)

the alloy $Ni_{62}Nb_{38}$, but also for $Ni_{59.2}Nb_{38.8}P_2$, indicating that the first phase is not completely destabilized by P-addition. This is supported by isothermal crystallization shown in Fig. 5, revealing similar crystallization signature in both alloys. This raises the question of which crystalline structure can be assigned to this first phase. Several studies have attributed it to the M-phase, similar to what has been observed in the ternary Ni–Nb–Al system [54–57]. The expected M-phase was simulated using the program VESTA [58] based on crystallographic data from Ref. [59], as shown in Fig. 6 (violet curve). However, the large number of Bragg peaks cannot be resolved in HE-XRD, as low-temperature crystallization typically involves homogeneous nucleation of crystals in the range of only few nanometers across the sample volume due to the strongly reduced dynamics, resulting in rather broad and diffuse instead of distinct reflexes. Consequently, identifying the M-phase by HE-XRD alone is not feasible. Nevertheless, studies by Collins et al. using transmission electron microscopy have conclusively shown that the M-phase is indeed the first crystallizing phase in binary Ni–Nb glass-forming alloys upon heating [56]. Given the similarity of the HE-XRD signature observed in the Ni–Nb system to that observed for Ni–Nb–P, it is reasonable to conclude that the M-phase also precipitates in the latter system.

Irrespective of whether the alloy is $Ni_{62}Nb_{38}$ or $Ni_{59.2}Nb_{38.8}P_2$, the phase that subsequently precipitates at T_{x2} corresponds to the formation of Ni_3Nb, one of the equilibrium phases. This phase is indicated by the appearance of a peak at Q-values around 3.1 Å^{-1}, which coincides with the most intense Bragg peaks in the simulated diffractogram of Ni_3Nb (represented by the red curve). When passing the second distinct exothermic reaction in the DSC, Ni_6Nb_7 forms, as evidenced by the appearance of the most prominent Bragg peaks of that phase at Q-values of 2.5 Å^{-1}, 2.8 Å^{-1} and 3.3 Å^{-1}. At elevated temperatures (T_{x4}, around 1200 K), the remaining metastable M-phase decomposes into Ni_3Nb and Ni_6Nb_7, resulting in a final structure composed exclusively of these two phases, at least in the case of the binary $Ni_{62}Nb_{38}$ alloy shown in Fig. 6a. These results match well with those observed for $Ni_{60}Nb_{40}$, which exhibits the same devitrification sequence from the glassy state to the formation of the equilibrium phases at higher temperatures [56]. In the case of $Ni_{59.2}Nb_{38.8}P_2$, however, the crystallization sequence is similar in its early stages up to T_{x3}, with the exception that an additional P-rich phase (Nb_3Ni_2P) emerges at high temperatures (T_{x4}), recognizable by the high-intensity Bragg peak at $Q = 2.8$ Å^{-1}. At this point, it should be mentioned that the identification of Bragg peaks in the in-situ HE-XRD measurements was challenging due to broad peak profiles, initially suggesting nanocrystalline domains. However, these features are primarily attributed to the limited resolution of the P21.1 beamline setup. To improve phase identification, additional ex-situ measurements were conducted at P21.2 after annealing the same compositions at three distinct crystallization temperatures. These measurements provided significantly higher peak resolution, enabling a more reliable assignment of the crystallizing phases, as shown in Fig. A.5 in the appendix.

The alloy $Ni_{59.2}Nb_{33.8}Ta_5P_2$ crystallizes analogously to the ternary alloy with the only difference that the metastable M-phase no longer forms, as shown in Fig. 6c. This was already indicated in the low temperature TTT diagrams, where the crystallization signature had changed from a double to a single crystallization event. This is mainly attributable to the inhibited atomic mobility, shifting the onset for crystallization to even higher temperatures and thus destabilizes the M-phase completely. Hence, the first phase that forms is Ni_3Nb at ~985 K (first crystallization event), followed by Ni_6Nb_7 (second crystallization event) and finally a P-rich phase at high temperatures. The individual regions are marked in the contour plot and selected diffractograms of the position marked in the DSC scan are shown in the right panel to provide a better overview of all phases. No phases containing Ta are indicated, however some Nb positions are likely occupied by Ta atoms due to their chemical similarity.

In addition to crystallization from the glassy state, the GFA is primarily determined during casting processes. Therefore, understanding the crystallization sequence upon cooling from the equilibrium liquid is crucial, particularly to assess the influence of P on the primary

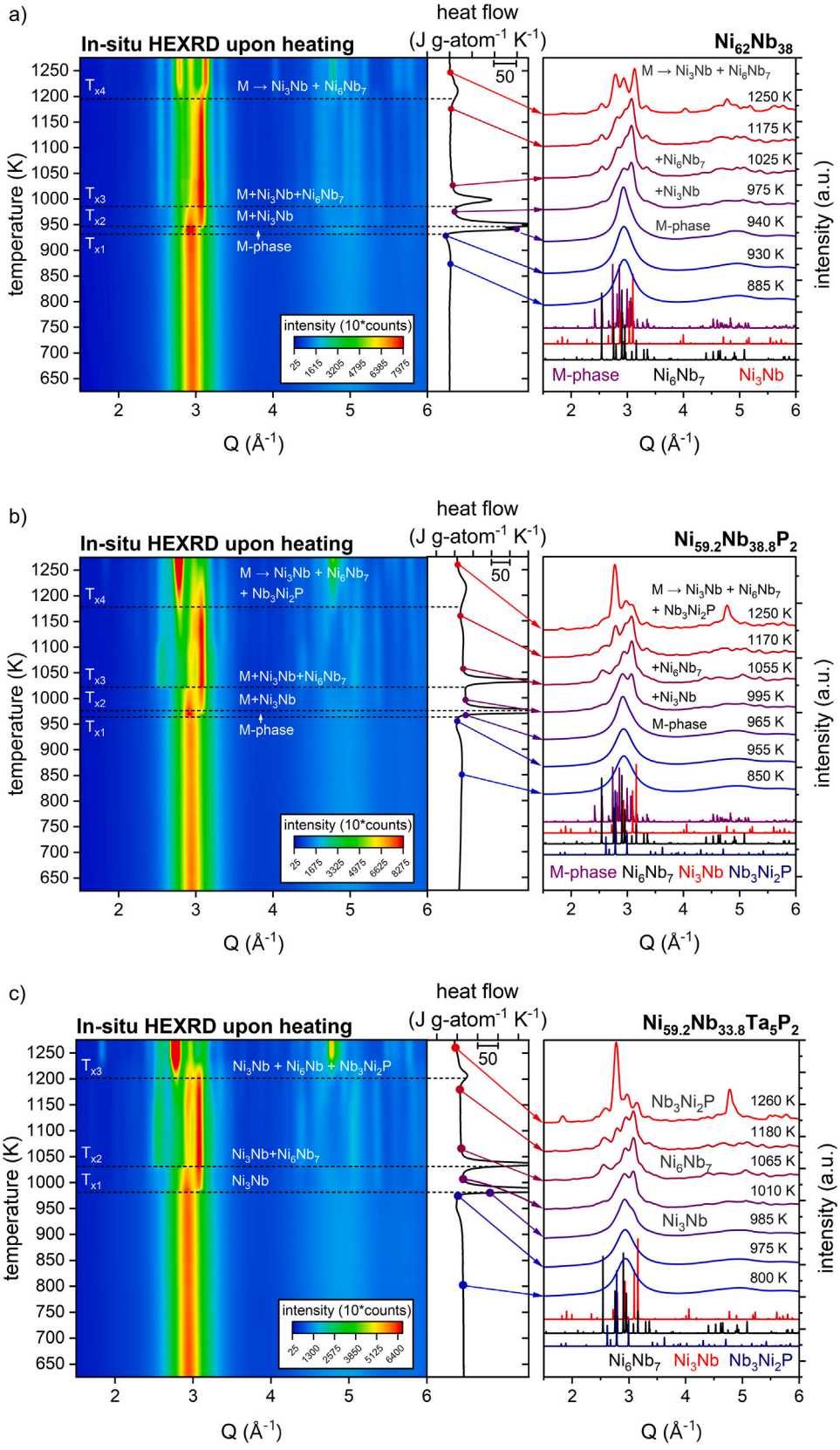

Fig. 6. In-situ HE-XRD results of (a) $Ni_{62}Nb_{38}$, (b) $Ni_{59.2}Nb_{38.8}P_2$ and (c) $Ni_{59.2}Nb_{33.8}Ta_5P_2$. Each figure is segmented into three parts. Left: Evolution of $I(Q)$ of an as-cast sample as a function of temperature in form of a contour plot. The various crystallization steps are marked from $T_{x,1}$ to $T_{x,4}$ with horizontally dotted lines. Middle: Corresponding DSC curve measured with the same heating rate as the HE-XRD measurements. Right: Detailed view of selected $I(Q)$ patterns showing the structural change starting from the amorphous state through the SCL up to the formation of the individual crystalline phases.

crystallizing phase. Containerless ESL HE-XRD experiments were conducted to investigate the crystallization sequence during free cooling of $Ni_{62}Nb_{38}$, $Ni_{59.2}Nb_{38.8}P_2$, and $Ni_{59.2}Nb_{33.8}Ta_5P_2$. Each composition was heated above the liquidus temperature and after switching off the heating laser, the diffraction patterns were recorded during free cooling of the samples. The contour plots in Fig. 7a, c and e show the temporal evolution of the diffraction patterns of one ESL processing cycle. The temperature was recorded with a pyrometer throughout the cycle, resulting in the temperature cooling profile shown in the left panel of Fig. 7b, d and f. Within these curves, different temperatures are indicated to cover all stages from equilibrium melt to the SCL as well as crystallization. These are marked as colored dots (color coding: red = high T, blue = low T) with the corresponding diffraction patterns shown in the right panel. The first appearance of a crystalline phase is marked at the respective temperature.

In the binary $Ni_{62}Nb_{38}$ alloy, a liquid amorphous structure exists between 1648 K (above the liquidus temperature, T_l) down to 1450 K, which corresponds to an undercooling of approximately 116 K. Primary crystallization of the orthorhombic Ni_3Nb phase initiates at 1460 K. The subsequent phase, trigonal Ni_6Nb_7, crystallizes at a slightly higher temperature of 1474 K due to the release of latent heat (recalescence), which is in agreement with the expected phase sequence based on the binary Ni–Nb phase diagram [60]. With the addition of P, the crystallization sequence changes, as can be seen in Fig. 7c and d. In addition to Ni_3Nb and Ni_6Nb_7, another phase emerges during the crystallization process. The formation of this phase is indicated by the appearance of new Bragg peaks at 1409 K (blue arrows), which occur simultaneously to Ni_3Nb (red arrows). However, since the levitation experiments were conducted in two separate campaigns, the phase identification of $Ni_{59.2}Nb_{38.8}P_2$ was more challenging due to the lower resolution of the diffraction data collected with the PerkinElmer detector (pixel size 200 μm) at P21.1 compared to those obtained with the Varex detector (pixel size 150 μm) at P21.2. Additionally, the improved Q-resolution at P21.2 was also related to the larger sample-to-detector distance (∼ 1.6 m at P21.2 compared to ∼0.6 m at P21.1), which reduced the angular spread per detector pixel and thus enabled more precise peak separation. Fig. A.5 in the appendix has already demonstrated the discrepancy in peak resolution between both beamlines. Despite this challenge, it is evident that the crystallization process clearly differs from that of the unmodified binary alloy. The alloy $Ni_{59.2}Nb_{33.8}Ta_5P_2$ provides a clearer picture, as shown in Fig. 7e and f (measured again at P21.2), where a new Nb-rich intermetallic with high phosphorus content (Nb_3Ni_2P [61]) crystallizes simultaneously to Ni_3Nb. The appearance of such an additional primary phase is not unexpected, as it is commonly observed upon micro-alloying of metalloids [62]. An in-depth assignment of this P-rich phase can be found in our previous study in Ref. [13]. Upon further cooling Ni_6Nb_7 additionally forms in all compositions. The only potential difference for the Ta-containing alloy may be that some of the Nb atom positions in the crystallizing phases are replaced by Ta following Vegard's law [63]. This is related to the fact that both elements are chemically and topologically equivalent. Furthermore, the Ni–Ta system exhibits identical pendants in terms of crystal structures due to their chemical similarities.

4. Discussion

The driving force for crystallization is represented by the Gibbs free energy difference ΔG_{l-x} between the liquid and the crystal, with high ΔG_{l-x} values, indicating a higher driving force for crystallization and hence a higher probability for nucleation. ΔG_{l-x} for Ni–Nb BMGs were determined based on molar heat capacity measurements being high, in particular when compared to other bulk glass-forming compositions. This is evident from Fig. 8, showing the T_l-scaled temperature-dependent $\Delta G_{l-x}(T)$ curves for various alloys. Since the obtainable data points in the SCL were limited due to the narrow SCLR, the driving force was additionally estimated based on the Turnbull approximation. This estimation requires information about the entropy of fusion ΔS_f, which can be calculated from the measured enthalpy of fusion ΔH_f and the liquidus temperature T_l, which are within the same range as the binary alloy measured by Mukherjee et al. [37]. This consistency supports the reliability of the results and confirms the observed high driving force for crystallization. However, the origin of a high GFA of a system does not solely rely on the driving force for crystallization, but also on various factors as elaborated by Gross et al. [64]. For instance, from a thermodynamic point of view, the interfacial energy between the liquid and crystal is another important factor that contributes to glass-formation. However, to estimate an interfacial energy (e.g. by JMAK fitting), the TTT diagram across the whole temperature range needs to be available. This is not the case for Ni–Nb-based alloys due to the high-temperature nature of this alloy family and the associated oxidation issues, as mentioned earlier. Although the interfacial energy cannot be directly determined, minor alloying may be an effective method to increase the liquid–crystal interfacial energy as postulated in Ref. [65], which could be a contributing factor to the observed increase in GFA from a thermodynamic point of view. Given that the liquid structure of Ni–Nb alloys is dominated by icosahedral motifs [66–69], as observed experimentally and by simulation for Ni–Nb-based alloys, a substantial structural mismatch with the primary precipitating phases characterized by their complex unit cells (orthorhombic Ni_3Nb and tetragonal Nb_3Ni_2P) is expected to result in a high interfacial energy. Therefore, despite having a high driving force for crystallization, Ni–Nb glasses may be thermodynamically stabilized by a high liquid–crystal interfacial energy. However, the thermodynamic contribution is not always the most important factor for glass formation, as systems such as Zr, Fe-, and Mg-based BMGs are rather stabilized from a kinetic point of view [70–73].

Such a slowdown in liquid dynamics appears to be decisive for glass formation in Ni–Nb alloys, which exhibit sluggish kinetics, particularly when P is present in the alloy. Fig. 9 presents viscosity data from low- and high-temperature measurements plotted against inverse temperature. It displays various fits, with both temperature ranges fitted separately using the VFT-model (dashed–dotted lines) and collectively using the extended MYEGA model (solid black line). The individual fits reveal a considerable difference in the temperature dependence of viscosity, showing a significantly more fragile behavior at high temperatures with $D^* = 6.6$ compared to $D^* = 13.9$ for $Ni_{62}Nb_{38}$ and $D^* = 17.2$ for $Ni_{59.2}Nb_{38.8}P_2$ at low temperatures. This contrast between a fragile high- and strong low-temperature liquid aligns with observations in numerous metallic glass-forming liquids and is linked to significant structural ordering during the cooling process [34,70,75–77]. A high-temperature fragile liquid tends to show less MRO, with its viscosity following a non-Arrhenius behavior. The transition from such an non-Arrhenius behavior to a 'quasi-Arrhenius' (rather linear) behavior, is thought to origin from the development of densely packed structures that create a more pronounced MRO [75,78]. This suggests that significant changes in the liquid structure are necessary to account for the sharp increase in viscosity, which is related to the change in liquid fragility, a phenomenon typically referred to as the fragile-to-strong transition. Similar behavior has been observed in a variety of glass-forming alloys, such as Zr-based [53,75,79], Fe-based [70,76] and La-based alloys [34], where the temperature dependence of viscosity also shifts from high fragility at high temperatures to low fragility at low temperatures. Such discrepancies are often observed when the VFT equation is used to model viscosity over several orders of magnitude. Therefore, it fails to properly describe the entire temperature range, prompting the use of alternative models. In this context, the extended MYEGA model is applied, consisting of two components that represent the strong low-temperature and fragile high-temperature regions. In simple terms, this model can be viewed as a combination of two VFT-functions into a single framework to accurately describe the viscosity behavior across various orders of magnitude. Therefore, the m-fragility values derived from the extended MYEGA fit (m = 54 and 49) closely

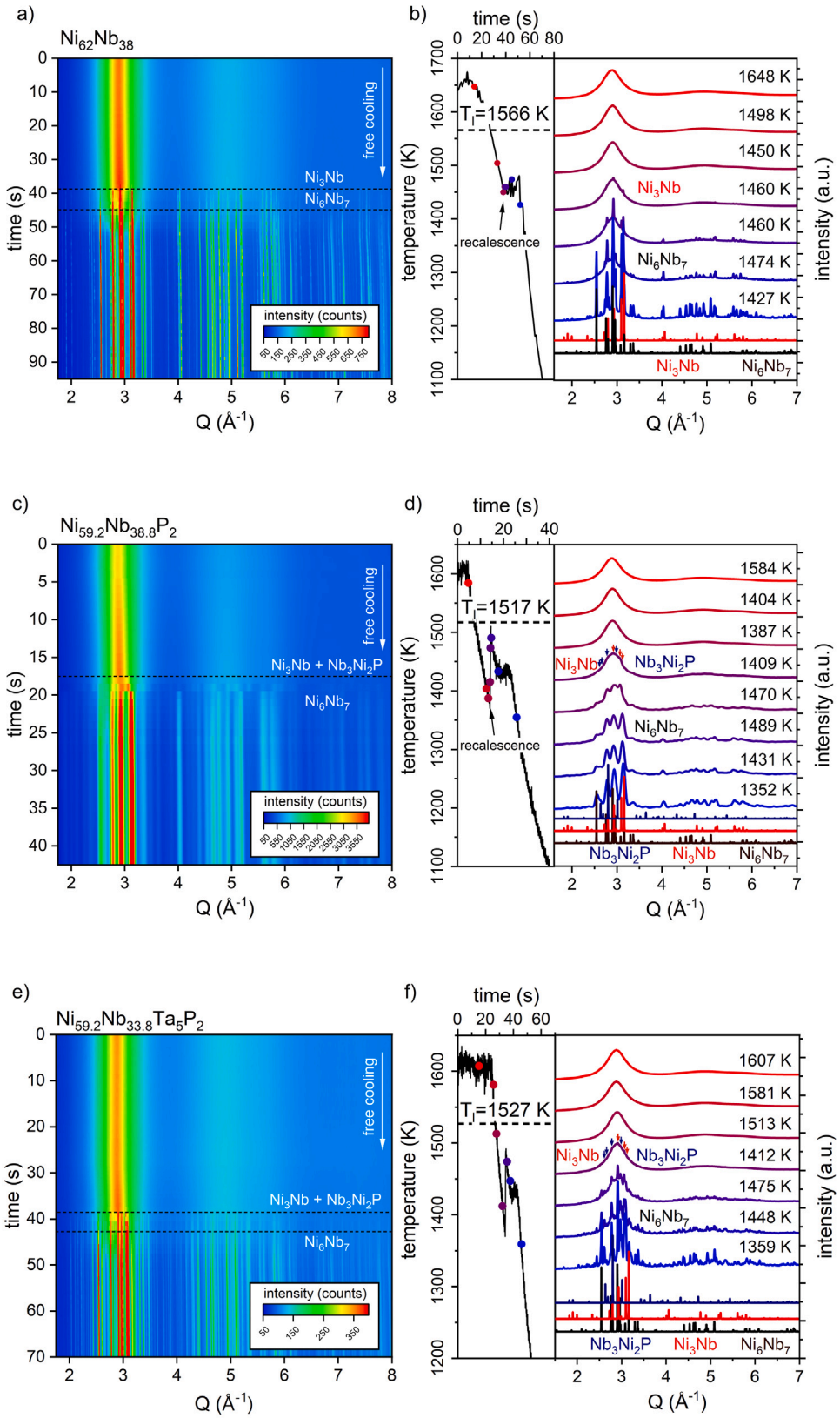

Fig. 7. (a), (b) and (c) depict the in-situ synchrotron HE-XRD sequence of $Ni_{62}Nb_{38}$, $Ni_{59.2}Nb_{38.8}P_2$ and $Ni_{59.2}Nb_{33.8}Ta_5P_2$, respectively, in particular the temporal evolution of the diffraction patterns of one cooling cycle. In (b), (d), and (f), the cooling curves and selected diffractograms reveal the structural changes occurring during the cycle. The data of binary $Ni_{62}Nb_{38}$ (a) have already been partly published in Ref. [13].

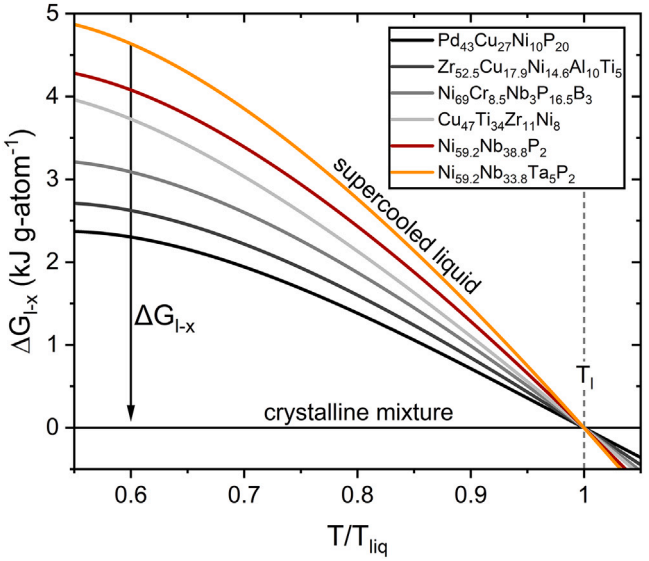

Fig. 8. Gibbs free energy difference ΔG_{l-x} between SCL and crystalline mixture normalized to the liquidus temperature T_l of Ni–Nb-(Ta)-P alloys compared to various other bulk glass-forming liquids. The data of those alloys are taken from Refs. [41,42,74].

Table 5
Summary of the extended MYEGA fitting parameters for Ni–Nb-(P) alloys. The kinetic glass transition temperature T_g^* and the fragility index m (slope at T_g^*) are derived from the extended MYEGA fit.

		$Ni_{62}Nb_{38}$		$Ni_{59.2}Nb_{38.8}P_2$	
		high T	low T	high T	low T
W_i	–	4.10	1.15×10^{-3}	200.46	1.01×10^{-3}
C_i	(K)	12 756.9	2439.7	17 855.5	2327.8
η_0	(10^{-2} Pas)	1.08		1.81	
T_g^*	(K)	901		914	
m	–	54		49	

match those obtained from individual VFT fitting (m = 60 and 52) for $Ni_{62}Nb_{38}$ and $Ni_{59.2}Nb_{38.8}P_2$. Overall, the key advantage of the extended MYEGA model is that it effectively addresses the FST. Furthermore, the viscosity prediction appears to be significantly more precise, closely aligning with data points at both high- and low-temperatures. In particular, the high-temperature data show good agreement, in contrast to the VFT-fit, which models those data less accurate, as is evident in the insets of Fig. 9. A summary of all fitting parameters, including the kinetic glass transition temperature T_g^* and m-fragility, can be found in Table 5.

To summarize the findings of the crystallization process, schematic TTT diagrams are constructed for the best binary, ternary, and quaternary Ni–Nb-based glass-forming compositions. These diagrams are based on the HE-XRD in-situ crystallization studies during heating and cooling, as well as critical casting size data for each composition. The objective is to provide a graphical visualization of the crystalline phase evolution on the basis of the alloying strategy. The diagram of the binary composition is shown in Fig. 10a, with the crystallization curve of Ni_3Nb (red curve) located at shorter times in comparison to Ni_6Nb_7 (black curve), corresponding to the phase sequence observed during continuous cooling from the liquid state. This is consistent with the phase sequence one would expect from the phase diagram (see Ref. [60]), as the composition is located on the Ni-rich side of the eutectic. The drawn cooling curves indicate a critical casting size of 2 mm, which means that casting at larger dimensions leads to crystallization, forming Ni_3Nb and Ni_6Nb_7. An estimate of the critical cooling rate can

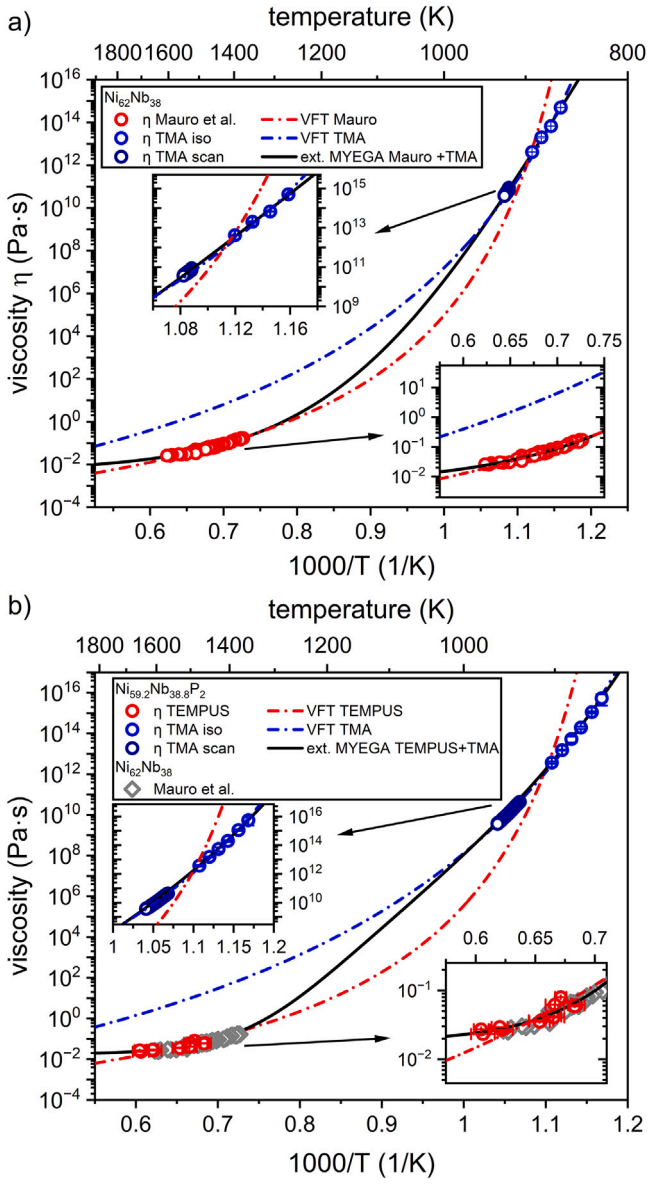

Fig. 9. Overview of the viscosity data across the whole temperature range for (a) $Ni_{62}Nb_{38}$ and (b) $Ni_{59.2}Nb_{38.8}P_2$. Viscosity data points from TMA measurements at low temperatures (scan: dark blue circles, isothermal: blue circles), electrostatic levitation experiments (taken from Ref. [50]), and TEMPUS experiments at high temperatures (red circles) are plotted over inverse temperature. In (b), the binary Ni–Nb high-temperature data are additionally shown to highlight that the addition of P does not significantly alter the viscosity of the high-temperature liquid. The data are fitted using the VFT model to describe the low- and high-temperature datasets individually, while the extended MYEGA model is able to describe the viscosity behavior across the entire temperature range. (For interpretation of the references to color in this figure legend, the reader is referred to the web version of this article.)

be calculated from the critical casting thickness d_c according to the empirical equation proposed by Lin et al. ($R = 10/d_c^2$, d_c in cm; R_c = 250 Ks^{-1}) [80]. Notably, the metastable M-phase (violet curve) is not encountered during cooling, but appears during crystallization upon heating from the glassy state. This phase subsequently decomposes into Ni_3Nb and Ni_6Nb_7, leaving a final structure composed of both eutectic phases analogous to the structure when crystallized during cooling. This is not only confirmed by the HE-XRD synchrotron data, but also

supported by the findings of Collins et al. who used electron microscopy to analyze a similar Ni–Nb alloy [56].

The effect of P on the crystallization curves of Ni_3Nb and Ni_6Nb_7 is shown in Fig. 10b (solid red and black lines), which shows that both phases shift to longer times due to a significant increase in GFA up to 5 mm. In addition, a P-rich compound forms alongside Ni_3Nb in P-containing alloys, which is not only observed for the $Ni_{59.2}Nb_{38.8}P_2$ composition, but also for $Ni_{59.2}Nb_{33.8}Ta_5P_2$. Similar changes in crystallization behavior were observed when S was introduced into the Ni–Nb system, leading to the precipitation of NiS, a compound highly enriched in S, analogous to the results of micro-alloying with P [81]. Further EDX analysis of the ESL-processed $(Ni_{62}Nb_{38})_{95}P_5$ sample, as presented in our previous study (Ref. [13]), revealed that the P solubility in the primary Ni_3Nb phase is close to zero, requiring long-range diffusion of P for crystal nucleation. This also applies to the formation of Nb_3Ni_2P, which requires significant local P enrichment in the liquid. As a result, at higher P concentrations (>2 at%), the liquid can more easily become enriched in P, promoting the nucleation of the P-rich primary phase, which reduces the GFA due to its higher nucleation tendency compared to the eutectic phases. However, when P is alloyed in optimized quantities (about 2 at%), the formation of Ni_3Nb is retarded due to the inability of Ni_3Nb to accommodate P in its crystalline structure, while it also reduces the melt dynamics, culminating in the observed enhancement of the critical casting size from 2 mm up to 5 mm [13]. This kinetic slowdown is also observable at low temperatures, as revealed by the stabilization of the SCL from initially no stable SCLR due to the formation of the M-phase to a broad SCLR of 49 K due to the partial destabilization of this phase. Considering the efficient cluster packing concept proposed by Miracle et al. [82], P is likely located in interstitial sites (octahedral or tetrahedral sites) within the densely packed amorphous structure, which reduces local free volume and lowers atomic mobility. This decreased mobility retards early-stage crystallization processes and thereby contributes to the observed suppression of the metastable M-phase during heating. This is further supported by the isothermal TTT experiments, which show that the onset for crystallization is shifted to longer times. Nevertheless, the M-phase still appears in the calorimetric signature as well as in the HE-XRD measurements, as shown in Fig. 5. Thus, the M-phase is shifted to higher temperatures, almost coinciding with the formation of Ni_3Nb, which is the subsequent crystallizing phase emerging from the glassy state.

As shown in Fig. 10c, the introduction of Ta into the Ni–Nb system does not alter the crystallization sequence substantially, with the Nb_3Ni_2P, $Ni_3(Nb,Ta)$ and $Ni_6(Nb,Ta)_7$ phases remaining almost unchanged during cooling. The main differences are found in the latter, which can be considered as mixtures of orthorhombic Ni_3Nb and Ni_3Ta as well as trigonal Ni_6Nb_7 and NiTa, as they exhibit identical crystal structures and are therefore miscible with each other. In addition, proper amounts of Ta shifts the crystallization 'noses' to even longer times, resulting in improved critical casting size up to 6 mm. This increase is coupled with improved kinetic stability, which is also reflected in the complete destabilization of the metastable M-phase in the low-temperature part of the TTT diagram, as confirmed by HE-XRD and DSC measurements. This improved kinetic stability is likely related to the atomic-size mismatch introduced by Ta, which slows long-range diffusion in the supercooled liquid, increases the nucleation barrier of metastable phases, thereby promoting direct crystallization into the thermodynamically stable equilibrium compounds. As a result, the SCLR is extended to a maximum of 60 K, which is the highest for these three alloys, demonstrating the beneficial effect of Ta on both phase stability and crystallization behavior in the Ni–Nb system.

5. Conclusion

This study demonstrates that the exceptional glass-forming ability of Ni–Nb-based bulk metallic glasses cannot be explained by thermodynamic driving forces alone. Despite a high Gibbs free energy difference

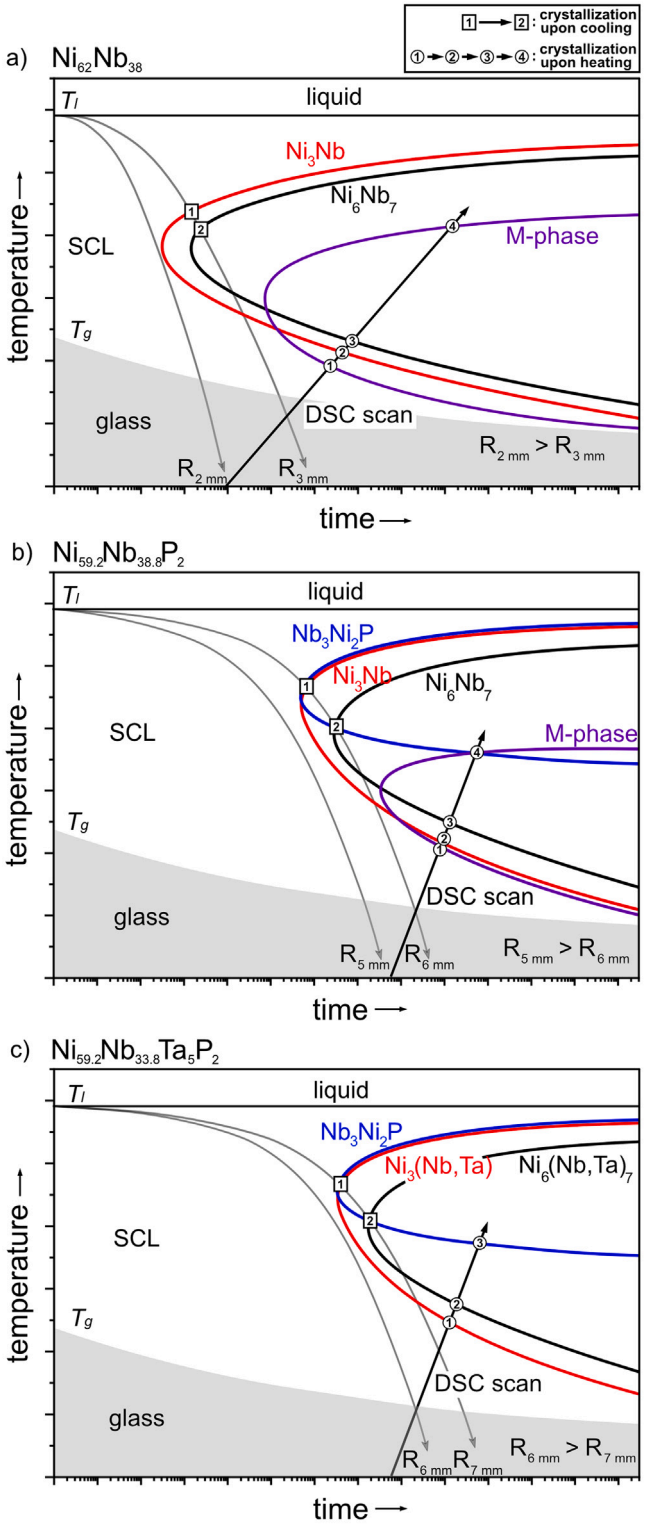

Fig. 10. Schematic TTT diagrams deduced from in-situ crystallization at high and low temperatures for (a) $Ni_{62}Nb_{38}$, (b) $Ni_{59.2}Nb_{38.8}P_2$ and (c) $Ni_{59.2}Nb_{33.8}Ta_5P_2$. The evolution of the crystallization curves can be observed from (a) to (c), which mainly reveals a shift to longer time scales as the GFA is improved from 2 mm to 5 mm for the P containing alloy and to 6 mm upon Ta addition. When P is present in the system, a P-rich Nb_3Ni_2P phase precipitates simultaneous to Ni_3Nb, resulting in the crystallization curves overlapping at high temperatures. Furthermore, no M-phase can be observed for the Ta-containing composition. *R* represents the cooling rate of the respective rod diameter.

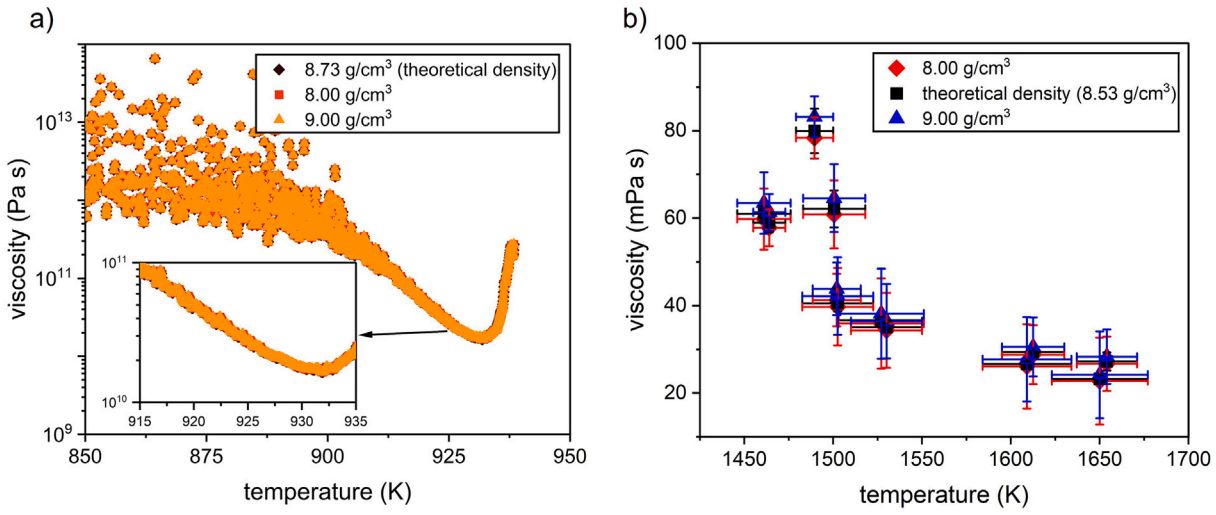

Fig. A.1. (a) Low-temperature viscosity calculated using the theoretical density in comparison to density values of 8.00 and 9.00 g cm^{-3}, spanning the expected density range of Ni–Nb alloys. The curves overlap, indicating negligible influence of density on the determined viscosity. (b) TEMPUS viscosities evaluated using the same density range, likewise showing no noticeable deviation from the theoretical-density result.

between the liquid and crystalline phases, indicative of a large nucleation probability, glass formation is favored due to kinetic stabilization and changes in the crystallization pathway. Minor additions of P and Ta significantly enhance the GFA by promoting a kinetic slowdown of the undercooled liquid and modifying the crystallization sequence. Viscosity measurements reveal a transition from fragile to strong liquid behavior during supercooling, indicating reduced atomic mobility and greater resistance to crystallization. The extended MYEGA model captures this behavior across a wide temperature range, providing a more accurate description compared to the conventional VFT model. From a structural perspective, the presence of icosahedral motifs in the liquid state and their mismatch with the crystalline phases (Ni_3Nb, Ni_6Nb_7, Nb_3Ni_2P) suggests a high liquid–crystal interfacial energy, which may raise the nucleation barrier and further stabilize the supercooled liquid. In-situ crystallization studies support this mechanism, showing delayed formation of eutectic and P-rich phases at moderate P levels, while excessive P contents favor simpler crystalline phases that reduce GFA. In summary, improved GFA results from a synergy of kinetic slowdown, structural mismatch and altered phase selection rather than a reduction in thermodynamic driving force. These findings highlight the effective role of microalloying with P in the Ni–Nb system in enhancing glass formation by modifying the crystallization pathway and reducing atomic mobility, while improvement from Ta is primarily attributed to additional kinetic slowdown resulting from atomic size mismatch and the confusion principle.

CRediT authorship contribution statement

Lucas M. Ruschel: Writing – original draft, Visualization, Validation, Supervision, Project administration, Methodology, Investigation, Formal analysis, Data curation, Conceptualization. **Bastian Adam:** Writing – review & editing, Investigation, Data curation. **Oliver Gross:** Writing – review & editing, Investigation, Data curation, Conceptualization. **Maximilian Frey:** Writing – review & editing, Investigation, Data curation. **Nico Neuber:** Writing – review & editing, Methodology, Data curation. **Fan Yang:** Writing – review & editing, Resources, Methodology, Investigation, Data curation. **Ralf Busch:** Writing – review & editing, Supervision, Project administration, Funding acquisition.

Declaration of competing interest

The authors declare that they have no known competing financial interests or personal relationships that could have appeared to influence the work reported in this paper.

Acknowledgments

The authors would like to thank F. Aubertin and I. Gallino for many fruitful discussions. We also thank DESY (Hamburg, Germany) for providing the experimental facilities. Parts of this research were performed at PETRA III at the P21.1 and P21.2 beamline facility, and we would like to thank Malte Blankenburg, Ulrich Lienert and Soham Banerjee for their support. Furthermore, we would like to thank the German Aerospace Center (DLR) for providing the electrostatic levitator setup for the in-situ synchrotron diffraction experiments, especially Dirk Holland-Moritz, Johanna Wilden, Lucas Kreuzer and Nicolai Grund who assisted during the campaign. Moreover, instrumentation and technical assistance for this work were provided by the Service Center X-ray Diffraction, with financial support from Saarland University, Germany and German Science Foundation (project number INST 256/349-1). The authors thank Dr. Oliver Janka for the support in collection of the X-ray diffraction data presented in this paper.

Appendix

A.1. Effect of theoretical density on viscosity results

To assess the influence of the assumed density on the low-temperature viscosity extracted from the TMA beam-bending method, the viscosity of $Ni_{62}Nb_{38}$ was recalculated using three density values: 8.00, 8.73, and 9.00 g cm^{-3}. The value of 8.73 g cm^{-3} corresponds to the theoretical density derived from the alloy composition, whereas the range 8.0–9.0 g cm^{-3} covers the values typically reported for amorphous (~ 8.6 g cm^{-3} [83]) and equilibrium liquid Ni–Nb alloys (~ 8.2–8.4 g cm^{-3}) in literature [37]. Fig. A.1 a) shows that the resulting viscosity curves are essentially indistinguishable over the relevant temperature interval, demonstrating that the TMA method is only weakly sensitive to variations in density and that the use of theoretical densities is sufficient for reliable viscosity determination. A similar analysis was performed for the viscosity obtained from the TEMPUS oscillating-drop method. Using the same density range (8.00 and 9.00 g cm^{-3}) resulted in viscosity values that overlap with those based on the theoretical density and remain well within the experimental uncertainty, as shown in Fig. A.1 b). This confirms that the influence of the assumed density on the TEMPUS-derived viscosity is also negligible.

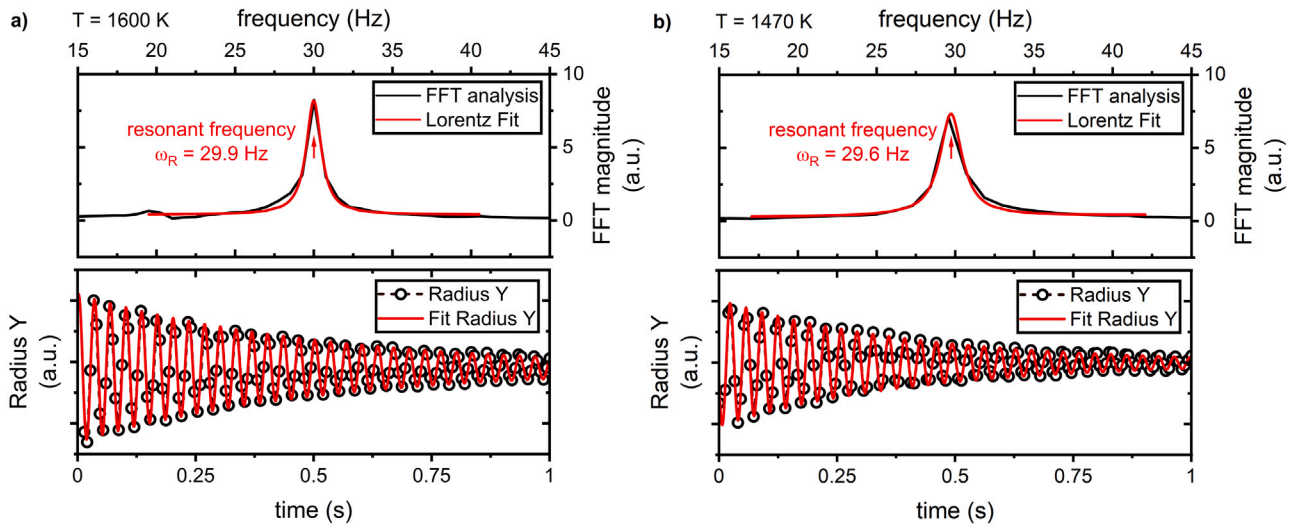

Fig. A.2. Change in the droplet radius in the Y-direction as a function of time after excitation, together with the corresponding frequency-domain obtained via Fast Fourier Transform (FFT) for two representative temperatures (T = 1470 K and T = 1600 K). The FFT reveals the dominant frequencies present in the damped oscillation and shows a single sharp peak at both temperatures, confirming strictly single-mode behavior.

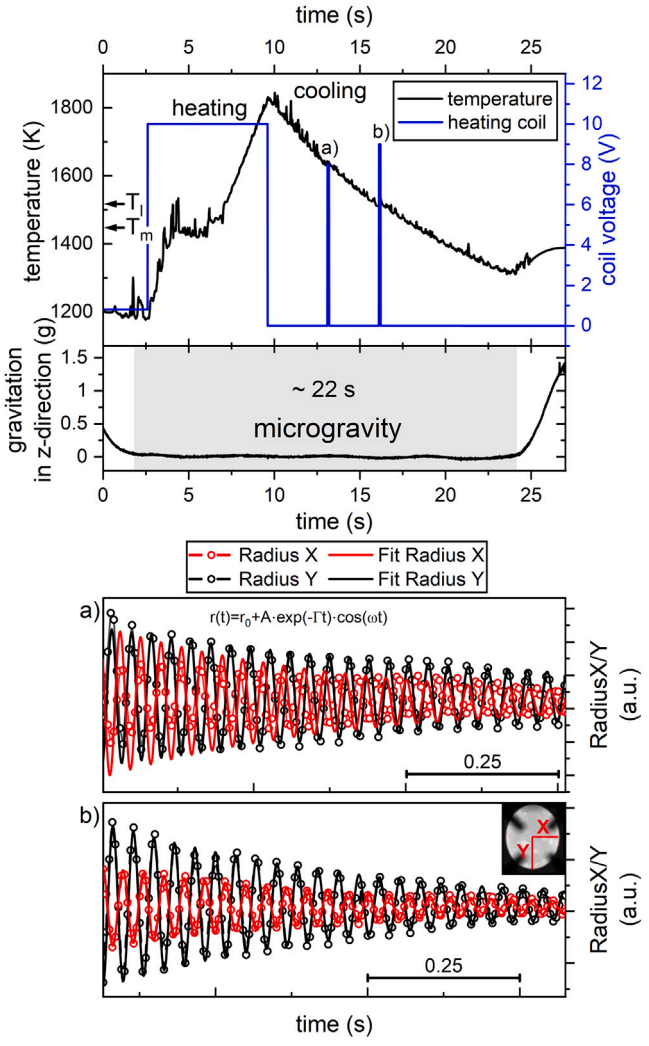

Fig. A.3. Temperature, coil voltage and gravitational force as a function of time for a single parabola. The spikes in the coil voltage correspond to the excitation pulses, labeled as (a) and (b). The resulting damped oscillations for each pulse are shown in panels (a) and (b) along the damped cosine fit.

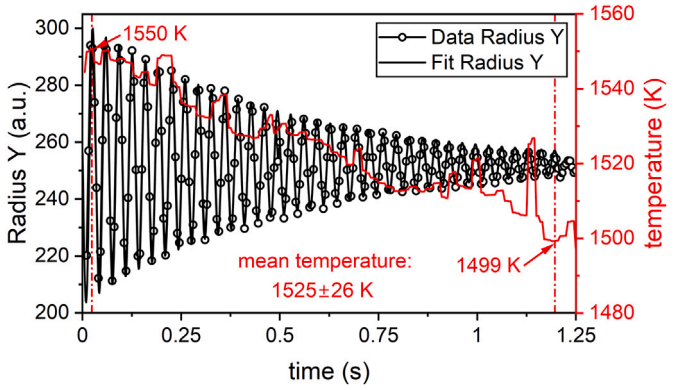

Fig. A.4. The black curve represents the droplet oscillation in Y-direction, while the red curve indicates the temperature drop due to the nature of the continuous cooling experiment. The average temperature is obtained from the start and end of the oscillation. (For interpretation of the references to color in this figure legend, the reader is referred to the web version of this article.)

A.2. TEMPUS evaluation

To verify that the oscillations used for the viscosity evaluation arise from a single well-defined oscillation, the recorded signals were transformed into the frequency domain using a Fast Fourier Transform. In this representation, coupled oscillations or surface-related nonlinearities would appear as secondary peaks. Representative spectra at 1470 K and 1600 K are shown in Fig. A.2. In both cases, a single resonance peak is observed, with no additional frequency components. The resonance frequency changes only slightly between the two temperatures (29.6 Hz to 29.9 Hz), indicating that the character of the oscillation remains effectively unchanged in the examined temperature interval. The frequency-domain analysis therefore confirms that the oscillations used for the viscosity determination correspond to a single oscillation and that the observed decay reflects viscous dissipation.

A typical process cycle of one parabola with the most important parameters of temperature, heating coil voltage and gravitational forces in *z*-direction as a function of time is shown in Fig. A.3. Two excitation pulses were applied to trigger an oscillation decay behavior, as shown in Fig. A.3a and b. The inset in Fig. A.3b depicts the initial excitation

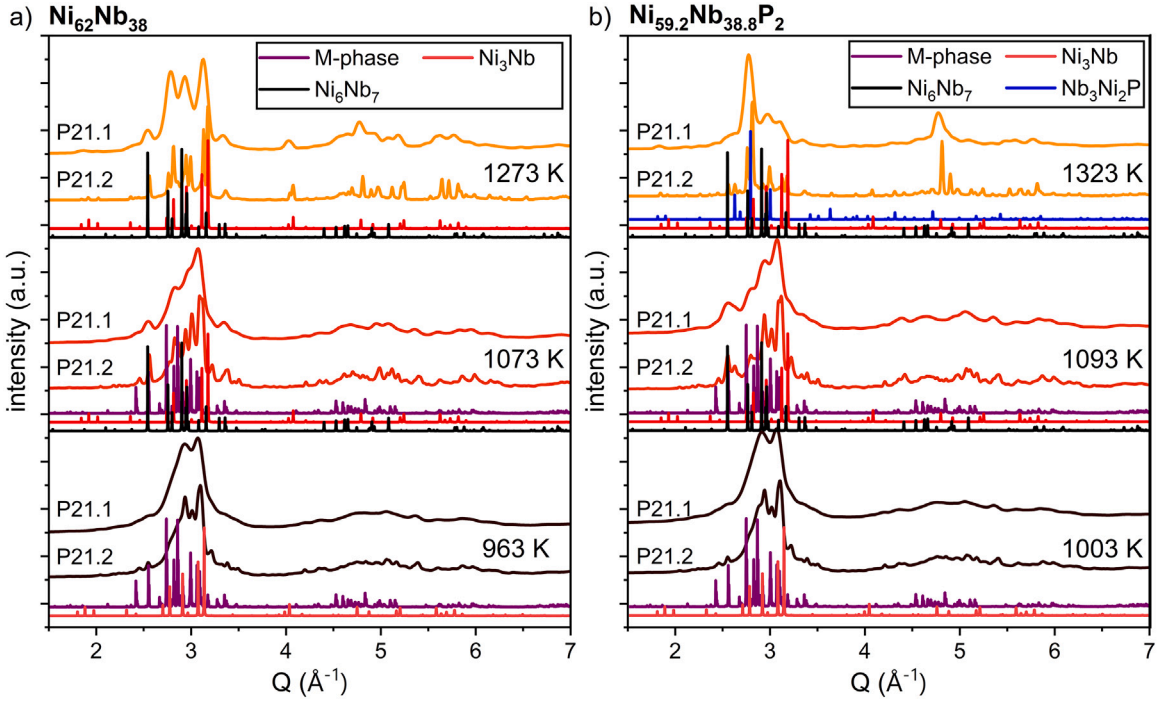

Fig. A.5. Comparison of the Bragg peak resolution between the DESY beamlines P21.1 and P21.2. The HE-XRD patterns of P21.1 were taken at the respective temperature from the in-situ scan measurements shown in Fig. 6, while the patterns of P21.2 were first annealed ex-situ at this temperature and then measured by HE-XRD at P21.1.

of the droplet, which decays over time as a result of internal friction of the sample.

Since the TEMPUS experiments are performed during continuous cooling, the viscosity values obtained represent an average over a specific temperature range. For instance, the onset of the oscillation shown in Fig. A.4 was identified at 1550 K, while it largely decayed at 1499 K. This results in an average temperature of 1525 K±26 K, which is regarded as the temperature error of this particular oscillation. It should be noted that the temperature error decreases with progressive cooling as oscillations decay faster due to the increase in viscosity. Moreover, the cooling rate has a shallower profile at lower temperatures, also reducing the temperature error.

A.3. HE-XRD resolution

The identification of Bragg peaks in low-temperature HE-XRD shown in Fig. 6 of the manuscript presented notable challenges due to the broad peak profiles, which initially suggested the presence of small crystallite sizes. However, these broad peaks are primarily attributed to the experimental setup at beamline P21.1. This becomes evident, when comparing those data to ex-situ measurements of the same compositions, which were additionally performed at beamline P21.2, as shown in Fig. A.5. These samples were first annealed in a DSC at three different temperatures, representing the crystalline state after each exothermic event (see Fig. 6 in the manuscript). The discrepancy in resolution between the two beamlines is striking and can be attributed to a number of factors, including the sample-detector distance, the beam energy, and the detector type. In order to achieve a Q-range of at least 15 $Å^{-1}$, the sample-to-detector distance varied between the two setups, with P21.2 employing a larger distance (~1.6 m) compared to P21.1 (~0.6 m) due to the different beam energies used. Beyond this difference in geometry, the improved resolution at P21.2 can also be attributed to advances in detector technology, in particular the smaller pixel size of the Varex detector (150 μm compared to 200 μm for the PerkinElmer detector at P21.1). This combination of larger sample-to-detector distance and smaller pixel size primarily contributed to the enhanced resolution of the diffraction patterns, thus considerably facilitating the identification of the crystallizing phases described above. Furthermore, this discrepancy in experimental resolution between the two beamlines is also evident for the crystallization sequence from the equilibrium liquid.

References

[1] A.L. Greer, E. Ma, Bulk Metallic Glasses: At the Cutting Edge of Metals Research, MRS Bull. 32 (08) (2007) 611–619, http://dx.doi.org/10.1557/mrs2007.121.

[2] M. Telford, The case for bulk metallic glass, Mater. Today 7 (3) (2004) 36–43, http://dx.doi.org/10.1016/S1369-7021(04)00124-5.

[3] R. Busch, The thermophysical properties of bulk metallic glass-forming liquids, JOM 52 (7) (2000) 39–42, http://dx.doi.org/10.1007/s11837-000-0160-7.

[4] R. Busch, J. Schroers, W.H. Wang, Thermodynamics and kinetics of bulk metallic glass, MRS Bull. 32 (8) (2007) 620–623, http://dx.doi.org/10.1557/mrs2007.122.

[5] R. Busch, I. Gallino, Kinetics, thermodynamics, and structure of bulk metallic glass forming liquids, JOM 69 (11) (2017) 2178–2186, http://dx.doi.org/10.1007/s11837-017-2574-5.

[6] Jong Hyun Na, Marios D. Demetriou, Michael Floyd, Andrew Hoff, Glenn R. Garrett, William L. Johnson, Compositional landscape for glass formation in metal alloys, Proc. Natl. Acad. Sci. 111 (25) (2014) 9031–9036, http://dx.doi.org/10.1073/pnas.1407780111, URL http://www.pnas.org/cgi/doi/10.1073/pnas.1407780111.

[7] H.T. Hu, L.Y. Chen, X.D. Wang, Q.P. Cao, J.Z. Jiang, Formation of Ni–Nb–Zr–X (X=Ti, Ta, Fe, Cu, Co) bulk metallic glasses, J. Alloys Compd. 460 (1–2) (2008) 714–718, http://dx.doi.org/10.1016/j.jallcom.2008.01.075.

[8] Zhengwang Zhu, Haifeng Zhang, Dagang Pan, Wensheng Sun, Zhuangqi Hu, Fabrication of binary Ni–Nb bulk metallic glass with high strength and compressive plasticity, Adv. Eng. Mater. 8 (10) (2006) 953–957, http://dx.doi.org/10.1002/adem.200600105, URL http://doi.wiley.com/10.1002/adem.200600105.

[9] S.L. Zhu, X.M. Wang, A. Inoue, Glass-forming ability and mechanical properties of Ti-based bulk glassy alloys with large diameters of up to 1 cm, Intermetallics 16 (8) (2008) 1031–1035, http://dx.doi.org/10.1016/j.intermet.2008.05.006.

[10] L. Xia, W.H. Li, S.S. Fang, B.C. Wei, Y.D. Dong, Binary Ni–Nb bulk metallic glasses, J. Appl. Phys. 99 (2) (2006) 026103, http://dx.doi.org/10.1063/1.2158130.

[11] H. Choi-Yim, D. Xu, W.L. Johnson, Ni-based bulk metallic glass formation in the Ni–Nb–Sn and Ni–Nb–Sn–X (X=B,Fe,Cu) alloy systems, Appl. Phys. Lett. 82 (7) (2003) 1030–1032, http://dx.doi.org/10.1063/1.1544434.

[12] L. Zhang, M.-J. Zhuo, J. Xu, Enhancing bulk metallic glass formation in Ni–Nb–Sn-based alloys via substitutional alloying with Co and Hf, J. Mater. Res. 23 (3) (2008) 688–699, http://dx.doi.org/10.1557/JMR.2008.0084.

[13] L.M. Ruschel, O. Gross, B. Bochtler, B. Li, B. Adam, N. Neuber, M. Frey, S. Jakovlev, F. Yang, H.-r. Jiang, B. Gludovatz, J.J. Kruzic, R. Busch, Ni–Nb–P-based bulk glass-forming alloys: Superior material properties combined in one alloy family, Acta Mater. 253 (January) (2023) 118968, http://dx.doi.org/10.1016/j.actamat.2023.118968.

[14] B. Li, L.M. Ruschel, K. Nomoto, O. Gross, B. Adam, N. Neuber, M. Frey, S.P. Ringer, B. Gludovatz, R. Busch, J.J. Kruzic, Fracture behavior of NiNb and NiNbP bulk metallic glasses, J. Alloys Compd. 1010 (August 2024) (2025) 177369, http://dx.doi.org/10.1016/j.jallcom.2024.177369.

[15] L.W. Crane, A.P. Bigg, Fracture toughness of high speed steels, Mater. Sci. Technol. 6 (10) (1990) 993–998, http://dx.doi.org/10.1179/026708390790189470.

[16] C. Kammer, Aluminum and aluminum alloys, in: Springer Handbooks, Springer International Publishing, 2018, pp. 161–197, http://dx.doi.org/10.1007/978-3-319-69743-7_6.

[17] R. Busch, W. Liu, W.L. Johnson, Thermodynamics and kinetics of the Mg65Cu25Y10 bulk metallic glass forming liquid, J. Appl. Phys. 83 (8) (1998) 4134–4141, http://dx.doi.org/10.1063/1.367167.

[18] B.A. Legg, J. Schroers, R. Busch, Thermodynamics, kinetics, and crystallization of Pt57.3Cu14.6Ni5.3P22.8 bulk metallic glass, Acta Mater. 55 (3) (2007) 1109–1116, http://dx.doi.org/10.1016/j.actamat.2006.09.024.

[19] H.E. Hagy, Experimental evaluation of beam-bending method of determining glass viscosities in the range 108 to 1015 poises, J. Am. Ceram. Soc. 46 (2) (1963) 93–97, http://dx.doi.org/10.1111/j.1151-2916.1963.tb11684.x.

[20] R. Kohlrausch, Theorie des elektrischen Rückstandes in der Leidener Flasche, Ann. Phys., Lpz. 167 (2) (1854) 179–214, http://dx.doi.org/10.1002/andp.18541670203.

[21] G. Williams, D.C. Watts, Non-symmetrical dielectric relaxation behaviour arising from a simple empirical decay function, Trans. Faraday Soc. 66 (1) (1970) 80, http://dx.doi.org/10.1039/tf9706600080.

[22] G. Lohoefer, Theory of an electromagnetically levitated metal sphere I: Absorbed power, SIAM J. Appl. Math. 49 (2) (1989) 567–581, http://dx.doi.org/10.1137/0149032.

[23] I. Egry, G. Lohöfer, I. Seyhan, S. Schneider, B. Feuerbacher, Viscosity and surface tension measurements in microgravity, Int. J. Thermophys. 20 (4) (1999) 1005–1015, http://dx.doi.org/10.1023/A:1022686316437.

[24] I. Egry, H. Giffard, S. Schneider, The oscillating drop technique revisited, Meas. Sci. Technol. 16 (2) (2005) 426–431, http://dx.doi.org/10.1088/0957-0233/16/2/013.

[25] G Lohöfer, M Beckers, T Blumberg, D Bräuer, S Schneider, T Volkmann, A Meyer, TEMPUS—A microgravity electromagnetic levitation facility for parabolic flights, Rev. Sci. Instrum. 95 (5) (2024) http://dx.doi.org/10.1063/5.0182719.

[26] G. Lohöfer, Viscosity measurement by the "oscillating drop" method: Limits of the linear model, Int. J. Thermophys. 46 (12) (2025) 193, http://dx.doi.org/10.1007/s10765-025-03618-1.

[27] R.K. Wunderlich, M. Mohr, Non-linear effects in the oscillating drop method for viscosity measurements, High Temp. - High Press. 48 (3) (2019) 253–277, http://dx.doi.org/10.32908/hthp.v48.648.

[28] H. Vogel, Das Temperaturabhaengigkeitsgesetz der Viskositaet von Fluessigkeiten, Phys. Z. 22 (1921) 645.

[29] G.S. Fulcher, Analysis of recent measurements of the viscosity of glasses, J. Am. Ceram. Soc. 75 (5) (1992) 1043–1055, http://dx.doi.org/10.1111/j.1151-2916.1992.tb05536.x.

[30] G. Tammann, W. Hesse, Die Abhaengigkeit der Viscosität von der Temperatur bie unterkuehlten Fluessigkeiten, Z. Für Anorg. Und Allg. Chem. 156 (1) (1926) 245–257, http://dx.doi.org/10.1002/zaac.19261560121.

[31] C.A. Angell, Formation of glasses from liquids and biopolymers, Science 267 (5206) (1995) 1924–1935, http://dx.doi.org/10.1126/science.267.5206.1924.

[32] S. Nemilov, Correlation of crystallization character of glass melts with the temperature dependence of their viscosity and the degree of spatial structural connectiveness, Glas. Phys. Chem. 21 (1995) 91–96, URL https://www.researchgate.net/publication/291929608.

[33] J.C. Mauro, Y. Yue, A.J. Ellison, P.K. Gupta, D.C. Allan, Viscosity of glass-forming liquids, Proc. Natl. Acad. Sci. 106 (47) (2009) 19780–19784, http://dx.doi.org/10.1073/pnas.0911705106.

[34] C. Zhang, L. Hu, Y. Yue, J.C. Mauro, Fragile-to-strong transition in metallic glass-forming liquids, J. Chem. Phys. 133 (1) (2010) http://dx.doi.org/10.1063/1.3457670.

[35] G. Ashiotis, A. Deschildre, Z. Nawaz, J.P. Wright, D. Karkoulis, F.E. Picca, J. Kieffer, The fast azimuthal integration Python library: pyFAI, J. Appl. Crystallogr. 48 (2) (2015) 510–519, http://dx.doi.org/10.1107/S1600576715004306.

[36] X. Qiu, J.W. Thompson, S.J.L. Billinge, PDFgetX2 : a GUI-driven program to obtain the pair distribution function from X-ray powder diffraction data, J. Appl. Crystallogr. 37 (4) (2004) http://dx.doi.org/10.1107/S0021889804011744, 678–678.

[37] S. Mukherjee, Z. Zhou, W.L. Johnson, W.-K. Rhim, Thermophysical properties of Ni–Nb and Ni–Nb–Sn bulk metallic glass-forming melts by containerless electrostatic levitation processing, J. Non-Cryst. Solids 337 (1) (2004) 21–28, http://dx.doi.org/10.1016/j.jnoncrysol.2004.03.102.

[38] C.T. Moynihan, A.J. Easteal, M.A. Bolt, J. Tucker, Dependence of the fictive temperature of glass on cooling rate, J. Am. Ceram. Soc. 59 (1–2) (1976) 12–16, http://dx.doi.org/10.1111/j.1151-2916.1976.tb09376.x.

[39] W. Kauzmann, The nature of the glassy state and the behavior of liquids at low temperatures, Chem. Rev. 43 (2) (1948) 219–256, http://dx.doi.org/10.1021/cr60135a002.

[40] S. Mukherjee, W.L. Johnson, W.K. Rhim, Noncontact measurement of high-temperature surface tension and viscosity of bulk metallic glass-forming alloys using the drop oscillation technique, Appl. Phys. Lett. 86 (1) (2005) http://dx.doi.org/10.1063/1.1844596.

[41] G.J. Fan, J.F. Löffler, R.K. Wunderlich, H.-J. Fecht, Thermodynamics, enthalpy relaxation and fragility of the bulk metallic glass-forming liquid Pd43Ni10Cu27P20, Acta Mater. 52 (3) (2004) 667–674, http://dx.doi.org/10.1016/j.actamat.2003.10.003.

[42] O. Gross, B. Bochtler, M. Stolpe, S. Hechler, W. Hembree, R. Busch, I. Gallino, The kinetic fragility of Pt-P- and Ni–P-based bulk glass-forming liquids and its thermodynamic and structural signature, Acta Mater. 132 (2017) 118–127, http://dx.doi.org/10.1016/j.actamat.2017.04.030.

[43] T.A. Waniuk, R. Busch, A. Masuhr, W.L. Johnson, Equilibrium viscosity of the Zr41.2Ti13.8Cu12.5Ni10Be22.5 bulk metallic glass-forming liquid and viscous flow during relaxation, phase separation, and primary crystallization, Acta Mater. 46 (15) (1998) 5229–5236, http://dx.doi.org/10.1016/S1359-6454(98)00242-0.

[44] D.H. Kim, W.T. Kim, E.S. Park, N. Mattern, J. Eckert, Phase separation in metallic glasses, Prog. Mater. Sci. 58 (8) (2013) 1103–1172, http://dx.doi.org/10.1016/j.pmatsci.2013.04.002.

[45] S. Lan, Y. Ren, X.Y. Wei, B. Wang, E.P. Gilbert, T. Shibayama, S. Watanabe, M. Ohnuma, X.L. Wang, Hidden amorphous phase and reentrant supercooled liquid in Pd–Ni–P metallic glasses, Nat. Commun. 8 (1) (2017) 14679, http://dx.doi.org/10.1038/ncomms14679.

[46] H.-R. Jiang, J.-y. Hu, N. Neuber, B. Bochtler, B. Adam, S.S. Riegler, M. Frey, L. Ruschel, W.-f. Lu, A.-h. Feng, R. Busch, J. Shen, Effect of sulfur on the glass-forming ability, phase transformation, and thermal stability of Cu-Zr-Al bulk metallic glass, Acta Mater. 212 (2021) 116923, http://dx.doi.org/10.1016/j.actamat.2021.116923.

[47] R. Busch, E. Bakke, W.L. Johnson, On the glass forming ability of bulk metallic glasses, Mater. Sci. Forum 235–238 (PART 1) (1996) 327–336, http://dx.doi.org/10.4028/www.scientific.net/MSF.235-238.327.

[48] W.H. Wang, Correlations between elastic moduli and properties in bulk metallic glasses, J. Appl. Phys. 99 (9) (2006) http://dx.doi.org/10.1063/1.2193060.

[49] L. Shadowspeaker, R. Busch, On the fragility of Nb-Ni-based and Zr-based bulk metallic glasses, Appl. Phys. Lett. 85 (13) (2004) 2508–2510, http://dx.doi.org/10.1063/1.1796523.

[50] N.A. Mauro, M. Blodgett, M.L. Johnson, A.J. Vogt, K.F. Kelton, A structural signature of liquid fragility, Nat. Commun. 5 (1) (2014) 4616, http://dx.doi.org/10.1038/ncomms5616.

[51] Z. Evenson, S. Raedersdorf, I. Gallino, R. Busch, Equilibrium viscosity of Zr–Cu–Ni–Al–Nb bulk metallic glasses, Scr. Mater. 63 (6) (2010) 573–576, http://dx.doi.org/10.1016/j.scriptamat.2010.06.008.

[52] Z. Evenson, I. Gallino, R. Busch, The effect of cooling rates on the apparent fragility of Zr-based bulk metallic glasses, J. Appl. Phys. 107 (12) (2010) 1–7, http://dx.doi.org/10.1063/1.3452381.

[53] M. Stolpe, I. Jonas, S. Wei, Z. Evenson, W. Hembree, F. Yang, A. Meyer, R. Busch, Structural changes during a liquid-liquid transition in the deeply undercooled Zr58.5Cu15.6Ni12.8Al10.3Nb2.8 bulk metallic glass forming melt, Phys. Rev. B 93 (1) (2016) 014201, http://dx.doi.org/10.1103/PhysRevB.93.014201.

[54] C.B. Shoemaker, D.P. Shoemaker, The crystal structure of the M phase, Nb–Ni–Al, Acta Crystallogr. 23 (2) (1967) 231–238, http://dx.doi.org/10.1107/S0365110X6700252X.

[55] R.C. Ruhl, B.C. Giessen, M. Cohen, N.J. Grant, New microcrystalline phases in the Nb–Ni and Ta–Ni systems, Acta Metall. 15 (11) (1967) 1693–1702, http://dx.doi.org/10.1016/0001-6160(67)90060-0.

[56] L.E. Collins, N.J. Grant, J.B. Vander Sande, Crystallization of amorphous Ni60Nb40, J. Mater. Sci. 18 (3) (1983) 804–814, http://dx.doi.org/10.1007/BF00745579.

[57] S. Stanojevic, I. Gallino, H. Aboulfadl, M. Sahin, F. Mücklich, R. Busch, Oxidation of glassy Ni–Nb–Sn alloys and its influence on the thermodynamics and kinetics of crystallization, Acta Mater. 102 (2016) 176–186, http://dx.doi.org/10.1016/j.actamat.2015.09.009.

[58] K. Momma, F. Izumi, VESTA : a three-dimensional visualization system for electronic and structural analysis, J. Appl. Crystallogr. 41 (3) (2008) 653–658, http://dx.doi.org/10.1107/S0021889808012016.

[59] Pierre Villars, Karin Cenzual (Eds.), Nb46Ni44Al10 (Nb6.13Ni5.52Al1.35) Crystal Structure: Datasheet from "PAULING FILE Multinaries Edition – 2022" in SpringerMaterials - Date accessed: 10.01.2025, Springer-Verlag Berlin Heidelberg and Material Phases Data System (MPDS), Switzerland & National Institute for Materials Science (NIMS), Japan, 2011, URL https://materials.springer.com/isp/crystallographic/docs/sd_0461581.

[60] H. Okamoto, Nb-Ni (Niobium–Nickel), J. Phase Equilibria Diffus. 29 (2) (2008) http://dx.doi.org/10.1007/s11669-008-9277-0, 210–210.

[61] Pierre Villars, Karin Cenzual (Eds.), Nb3Ni2P (Nb2.5Ni1.66P0.84) Crystal Structure: Datasheet from "PAULING FILE Multinaries Edition – 2012" in SpringerMaterials - Date accessed: 10.01.2025, Springer-Verlag Berlin Heidelberg and Material Phases Data System (MPDS), Switzerland and National Institute for Materials Science (NIMS), Japan, 2011, URL https://materials.springer.com/isp/crystallographic/docs/sd_0540203.

[62] W.H. Wang, Roles of minor additions in formation and properties of bulk metallic glasses, Prog. Mater. Sci. 52 (4) (2007) 540–596, http://dx.doi.org/10.1016/j.pmatsci.2006.07.003.

[63] L. Vegard, Die Konstitution der Mischkristalle und die Raumfüllung der Atome, Z. Für Phys. 5 (1) (1921) 17–26, http://dx.doi.org/10.1007/BF01349680.

[64] O. Gross, Precious Metal Based Bulk Glass-Forming Liquids: Development, Thermodynamics, Kinetics and Structure (Ph.D. thesis), Saarland University, Dissertation, 2018.

[65] O. Gross, S.S. Riegler, M. Stolpe, B. Bochtler, A. Kuball, S. Hechler, R. Busch, I. Gallino, On the high glass-forming ability of Pt–Cu–Ni/Co–P-based liquids, Acta Mater. 141 (2017) 109–119, http://dx.doi.org/10.1016/j.actamat.2017.09.013.

[66] N.A. Mauro, M.L. Johnson, J.C. Bendert, K.F. Kelton, Structural evolution in Ni–Nb and Ni–Nb–Ta liquids and glasses — A measure of liquid fragility? J. Non-Cryst. Solids 362 (1) (2013) 237–245, http://dx.doi.org/10.1016/j.jnoncrysol.2012.11.022.

[67] K. Vijay Reddy, S. Pal, Contribution of Nb towards enhancement of glass forming ability and plasticity of Ni–Nb binary metallic glass, J. Non-Cryst. Solids 471 (June) (2017) 243–250, http://dx.doi.org/10.1016/j.jnoncrysol.2017.06.007.

[68] T.D. Xu, X.D. Wang, H. Zhang, Q.P. Cao, D.X. Zhang, J.Z. Jiang, Structural evolution and atomic dynamics in Ni–Nb metallic glasses: A molecular dynamics study, J. Chem. Phys. 147 (14) (2017) 144503, http://dx.doi.org/10.1063/1.4995006.

[69] W. Lu, J.-C. Tseng, A. Feng, J. Shen, Structural origin of the enhancement in glass-forming ability of binary Ni–Nb metallic glasses, J. Non-Cryst. Solids 564 (January) (2021) 120834, http://dx.doi.org/10.1016/j.jnoncrysol.2021.120834.

[70] B. Bochtler, O. Gross, I. Gallino, R. Busch, Thermo-physical characterization of the Fe67Mo6Ni3.5Cr3.5P12C5.5B2.5 bulk metallic glass forming alloy, Acta Mater. 118 (2016) 129–139, http://dx.doi.org/10.1016/j.actamat.2016.07.031.

[71] S. Mukherjee, J. Schroers, W.L. Johnson, W.-K. Rhim, Influence of kinetic and thermodynamic factors on the glass-forming ability of zirconium-based bulk amorphous alloys, Phys. Rev. Lett. 94 (24) (2005) 245501, http://dx.doi.org/10.1103/PhysRevLett.94.245501.

[72] M. Frey, R. Busch, W. Possart, I. Gallino, On the thermodynamics, kinetics, and sub-Tg relaxations of Mg-based bulk metallic glasses, Acta Mater. 155 (2018) 117–127, http://dx.doi.org/10.1016/j.actamat.2018.05.063.

[73] R. Busch, W. Liu, W.L. Johnson, Thermodynamics and kinetics of the Mg65Cu25Y10 bulk metallic glass forming liquid, J. Appl. Phys. 83 (8) (1998) 4134–4141, http://dx.doi.org/10.1063/1.367167.

[74] B. Bochtler, Thermophysical and Structural Investigations of a CuTi- and a Zr-based Bulk Metallic Glass, the Influence of Minor Additions, and the Relation to Thermoplastic Forming (Ph.D. thesis), Saarland University, 2019.

[75] Z. Evenson, T. Schmitt, M. Nicola, I. Gallino, R. Busch, High temperature melt viscosity and fragile to strong transition in Zr–Cu–Ni–Al–Nb(Ti) and Cu47Ti34Zr11Ni8 bulk metallic glasses, Acta Mater. 60 (12) (2012) 4712–4719, http://dx.doi.org/10.1016/j.actamat.2012.05.019.

[76] B. Bochtler, O. Gross, R. Busch, Indications for a fragile-to-strong transition in the high- and low-temperature viscosity of the Fe 43 Cr 16 Mo 16 C 15 B 10 bulk metallic glass-forming alloy, Appl. Phys. Lett. 111 (26) (2017) 261902, http://dx.doi.org/10.1063/1.5013108.

[77] S. Wei, M. Stolpe, O. Gross, W. Hembree, S. Hechler, J. Bednarcik, R. Busch, P. Lucas, Structural evolution on medium-range-order during the fragile-strong transition in Ge15Te85, Acta Mater. 129 (2017) 259–267, http://dx.doi.org/10.1016/j.actamat.2017.02.055.

[78] C. Zhou, L. Hu, Q. Sun, H. Zheng, C. Zhang, Y. Yue, Structural evolution during fragile-to-strong transition in CuZr(Al) glass-forming liquids, J. Chem. Phys. 142 (6) (2015) 064508, http://dx.doi.org/10.1063/1.4907374.

[79] S. Wei, F. Yang, J. Bednarcik, I. Kaban, O. Shuleshova, A. Meyer, R. Busch, Liquid–liquid transition in a strong bulk metallic glass-forming liquid, Nat. Commun. 4 (1) (2013) 2083, http://dx.doi.org/10.1038/ncomms3083.

[80] X.H. Lin, W.L. Johnson, Formation of Ti–Zr–Cu–Ni bulk metallic glasses, J. Appl. Phys. 78 (11) (1995) 6514–6519, http://dx.doi.org/10.1063/1.360537.

[81] N. Grund, D. Holland-Moritz, S. Khademorezaian, L.P. Kreuzer, N. Neuber, L.M. Ruschel, H. Voigt, J. Wilden, F. Yang, S. Banerjee, M. Blankenburg, A.C. Dippel, J.P. Embs, S. Divinski, R. Busch, A. Meyer, G. Wilde, Impact of sulfur addition on the structure and dynamics of Ni–Nb alloy melts, APL Mater. 12 (5) (2024) http://dx.doi.org/10.1063/5.0205058.

[82] D.B. Miracle, D.V. Louzguine-Luzgin, L.V. Louzguina-Luzgina, A. Inoue, An assessment of binary metallic glasses: correlations between structure, glass forming ability and stability, Int. Mater. Rev. 55 (4) (2010) 218–256, http://dx.doi.org/10.1179/095066010X12646898728200.

[83] Xiang-Yuan Cui, Simon P. Ringer, Gang Wang, Z.H. Stachurski, What should the density of amorphous solids be? J. Chem. Phys. 151 (19) (2019) http://dx.doi.org/10.1063/1.5113733.